Geosci. Model Dev. Discuss., 8, 7911–7981, 2015
www.geosci-model-dev-discuss.net/8/7911/2015/
doi:10.5194/gmdd-8-7911-2015

Geoscientific Model Development Discussions

VISIR-I: small vessels, least-time nautical routes using wave forecasts

G. Mannarini[1], N. Pinardi[1,2,3], G. Coppini[1], P. Oddo[2,a], and A. Iafrati[4]

[1]Centro Euro–Mediterraneo sui Cambiamenti Climatici – Ocean Predictions and Applications, via Augusto Imperatore 16, 73100 Lecce, Italy
[2]Istituto Nazionale di Geofisica e Vulcanologia, Via Donato Creti 12, 40100 Bologna, Italy
[3]Università degli Studi di Bologna, viale Berti-Pichat, 40126 Bologna, Italy
[4]CNR-INSEAN, Via di Vallerano 139, 00128 Roma, Italy
[a]presently at: NATO Science and Technology Organisation – Centre for Maritime Research and Experimentation, Viale San Bartolomeo 400, 19126 La Spezia, Italy

Received: 1 August 2015 – Accepted: 14 August 2015 – Published: 11 September 2015

Correspondence to: G. Mannarini (gianandrea.mannarini@cmcc.it)

Published by Copernicus Publications on behalf of the European Geosciences Union.

Abstract

A new numerical model for the on-demand computation of optimal ship routes based on sea-state forecasts has been developed. The model, named VISIR (discoVerIng Safe and effIcient Routes) is designed to support decision-makers when planning a marine voyage.

The first version of the system, VISIR-I, considers medium and small motor vessels with lengths of up to a few tens of meters and a displacement hull. The model is made up of three components: the route optimization algorithm, the mechanical model of the ship, and the environmental fields. The optimization algorithm is based on a graph-search method with time-dependent edge weights. The algorithm is also able to compute a voluntary ship speed reduction. The ship model accounts for calm water and added wave resistance by making use of just the principal particulars of the vessel as input parameters. The system also checks the optimal route for parametric roll, pure loss of stability, and surfriding/broaching-to hazard conditions. Significant wave height, wave spectrum peak period, and wave direction forecast fields are employed as an input.

Examples of VISIR-I routes in the Mediterranean Sea are provided. The optimal route may be longer in terms of miles sailed and yet it is faster and safer than the geodetic route between the same departure and arrival locations. Route diversions result from the safety constraints and the fact that the algorithm takes into account the full temporal evolution and spatial variability of the environmental fields.

1 Introduction

The operational availability of high spatial and temporal resolution forecasts, for both weather, sea-state and oceanographic variables opens the way to a realm of downstream services, which are increasingly closer to end-user needs (Proctor and Howarth, 2008). Such services may support the decisional process in critical situations

where knowledge of the present and predicted environmental state is key to avoiding casualties or to making savings in terms of time, cost, or environmental impact.

VISIR [vi'zi:r][1] is a model and an operational system[2] for the on-demand computation of safe and efficient ship routes, based on sea-state forecasts. In its present version, VISIR-I, medium and small motor vessels with displacement hulls are considered, such as: fishing vessels (e.g. seiners, trawlers), towboats and fireboats, service boats (crew and supply boats), short trip coastal freighters, displacement hull yachts and pleasure crafts, and small ferry boats.

The aim of this paper is to lay a sound scientific foundation of VISIR-I, including all its main components: the optimization algorithm, the ship model, and the processing of the environmental fields.

After reviewing the literature in Sect. 1.1 and summarizing our original contribution in Sect. 1.2, the solution devised for VISIR-I is presented in detail in Sect. 2. Examples of optimal routes in the Mediterranean Sea, (Sect. 3), precede the conclusions, which are drawn in Sect. 4.

1.1 Review of literature

The main mathematical schemes available in the literature to solve ship routing problems are reviewed in the following.

Initially devised as a manual tool for navigators, the isochrone method is based on the idea of building an envelope of positions attainable by a vessel at a given time lag after departure. This envelope is called an "isochrone". In the work by Hagiwara (1989), a detailed algorithm is provided, describing how to generate the isochrones and how to use them for constructing a least-time route. Space and course discretization in the vicinity of the rhumb line between departure and arrival locations are performed. At

[1] "Visir" is the Italian for "vizier", who was a high-ranking political advisor in the Arab world. Its etymology seems to be related to the ideas of "deciding" and "supporting".

[2] http://www.visir-nav.com/

each progress stage, the course leading to the maximum spatial advancement from the origin is considered. When an isochrone gets close enough to the destination, the optimal route is recovered by a backtracking procedure. No proof of the time-optimality of the resulting route is provided. Hagiwara's modified isochrone method is the basis for the fuel optimization method proposed by Klompstra et al. (1992). Here, each stage is represented by a two-dimensional position and time. Instead of isochrones or time-fronts, energy-fronts or "isopones" are computed, being the attainable regions for a given expenditure on fuel. Szlapczynska and Smierzchalski (2007) review several variants of the isochrone method, highlighting their weaknesses, such as limitations in the form of ship speed characteristics and in dealing with landmasses, especially in the vicinity of narrow straits. The authors propose a solution to the latter issue, by screening all route portions intersecting the landmass.

The variational approach involves searching for trajectories making an objective functional stationary, such as total time of navigation or operational cost, given a set of constraints. The search is achieved by varying the parameters controlling the trajectory. This approach is equivalent to solving the Euler–Lagrange equation. In Hamilton (1962), least-time ship routes are computed by varying the ship's course, under the assumption that the environmental field is static and thus vessel speed does not explicitly depend on time.

The time-dependent problem instead can be addressed through the technique of optimal control (Pontriagin et al., 1962). With this method, the dynamic system (the vessel) is controlled by a time-dependent input function (typically engine thrust and rudder angle), allowing the objective function to be minimized. Optimal control is formulated in terms of a set of necessary conditions (Luenberger, 1979). Applications of optimal control to ship routing problems are found in Bijlsma (1975), Perakis and Papadakis (1989) and Techy (2011). Least-time transatlantic routes are computed by Bijlsma (1975). There, significant wave height and wave direction fields from 12 hourly forecasts are assumed to determine vessel speed, while the sole control variable is vessel course. The method can account for prohibited courses due to dynamic rea-

sons (e.g. rolling). However, specific geometrical conditions on the vessel speed characteristics have to hold for the method to work. Furthermore, due to topological issues, there are unreachable regions of the ocean, and the method involves guessing the initial vessel course, which may hinder the implementation in an automated system. The approach by Perakis and Papadakis (1989) accounts for a delayed departure time and for passage through an intermediate location (point-constrained problem). Local optimality conditions ("broken extremals") are found at the boundaries of spatial subdomains. The optimal ship power setting is found to always take the maximum value possible. The results hold under the assumption that the ship speed characteristics depend on engine throttle as a multiplicative factor. Another limitation of this approach is that the computed extremal trajectory is not guaranteed to lead to a minimum of the objective function (instead a maximum could be retrieved). In Techy (2011) the author reports on a vessel moving with constant velocity with respect to water in presence of currents ("Zermelo's problem"). The optimal trajectory is analyzed as a function of flow divergence and vorticity, finding the optimal steering policy in a point-symmetric, time-varying flow field. In addition, a geometrical interpretation of Pontriagin's principle is provided. However, to deliver a unique solution, the method requires the hypothesis that the domain of maneuverability of the ship is convex.

The work by Lolla et al. (2014) is based on the computation of the reachability front of a vehicle with an internal propulsion system, subject to a time-dependent ocean flow. The front is implicitly defined through a level set, and its evolution satisfies a specific solution of a Hamilton–Jacobi equation. The optimal speed of the vehicle is found to always take the maximum value admissible. The actual trajectory is computed via backtracking. This approach allows for both stationary and mobile obstacles, and is able to compute an optimal departure time for the vehicle. The use of generalized gradients and co-states overcome the hypothesis of regularities of the level set. This promising method is at present still lacking an operational implementation.

Monte Carlo methods discard exact solutions in favour of faster solutions. Also, they provide a viable technique for fulfilling multiple and competing objectives. A class of

Monte Carlo methods makes use of genetic algorithms. They start with guessed routes ("chromosomes") whose subparts ("genes") cross each other and mutate in a random way, in order to find a new route ("offspring") that better fits the objective function of the actual problem. The use of Monte Carlo methods in the context of multi-objective optimization is reviewed in Konak et al. (2006), while an application to ship routing is provided by Szlapczynska (2007). There is also a simulated annealing approach to ship routing (Kosmas and Vlachos, 2012). In this case, in order to find a global optimum a trial route is perturbed in a statistical-mechanical fashion. Given that in Monte Carlo methods there is no exact analytical solution, additional criteria are needed in order to decide whether a solution is satisfactory ("convergence test").

In discrete methods, the spatial domain is represented by some kind of grid (regular or not) and the optimization is based on recursive schemes. A key concept is the so called principle of optimality: given a point on the optimal trajectory, the remaining trajectory is optimal for the minimization problem initiated at that point (Luenberger, 1979). This property can be stated as a recursive relation, called "Bellman's condition" in the framework of discrete methods. In Zoppoli (1972) a dynamic programming method for the computation of a least-time ship route in the Indian Ocean is used. The algorithm is able to ingest time-dependent environmental fields, by evaluating them at the nearest quantized time value. However, the actual case-study provided in the paper just uses stationary fields. Ship operating costs for transatlantic routes are minimized in Chen (1978), where a terminal cost is also included in the objective function. The grid used however is just a band of gridpoints along the rhumb-line track, thus being limited in terms of application when there are complex topological constraints, such as in a coastal environment. Takashima et al. (2009) use dynamic programming for computing minimum fuel routes of a given duration in time. The propeller revolution number is kept constant during the voyage and its value is adjusted in order to reach the target route duration. The ship course is varied in order to exploit ocean currents. However, the algorithm uses static environmental information, and re-routing is run every three hours in order to deal with dynamic currents. The dynamic programming method by

Wei and Zou (2012) is used to minimize fuel consumption. Both throttle and heading of the vessel can be optimized, again with grid limitations as in Chen (1978). Montes (2005) employs Dijkstra's algorithm to compute least-time routes in time-varying forecast fields. However, the effect of weather on vessel speed is parametrized in terms of subjective parameters ("speed penalty function").

1.2 Our contribution

There are several recurrent shortcomings in the ship routing literature: the limited capability to deal with complex topological conditions, such as in the coastal environment (Bijlsma, 1975; Hagiwara, 1989; Szlapczynska and Smierzchalski, 2007); the need for heuristics or subjective parameters in the optimization algorithm (Kosmas and Vlachos, 2012; Montes, 2005); non explicit use of time-dependent environmental information (Hamilton, 1962; Zoppoli, 1972; Takashima et al., 2009); limitations on the functional dependence of the vessel response function (Perakis and Papadakis, 1989; Techy, 2011); and the not yet demonstrated use in an operational environment (Lolla et al., 2014).

All these issues need to be addressed simultaneously by a model aimed at feeding an operational system that also works in coastal waters, for a wide class of vessels and environmental conditions, taking into account navigation safety according to the latest international standards. In VISIR-I all the above mentioned shortcomings are overcome. The method is based on an exact graph search algorithm, modified in order to manage time-dependent environmental fields and voluntary vessel speed reduction. It is validated against analytical results. In addition, the graph grid is designed to deal with the topological requirements of coastal navigation. VISIR-I also includes a dedicated motorboat model and safety constraints for vessel intact stability are considered.

All these features are described in detail in what follows.

2 VISIR-I method

In this section we present the method employed by VISIR-I for solving the route optimization problem. First, the problem is formally stated (Sect. 2.1), then the solution algorithm (Sect. 2.2), the mechanical model of the ship (Sect. 2.3) and the processing of the environmental analysis and forecast fields affecting the ship dynamics (Sect. 2.4) are presented. The structure of the computer code is provided in Sect. 2.5 and a validation of the resulting optimal routes is given in Sect. 2.6.

2.1 Statement of the problem

The mathematical problem addressed and solved in an operational way by VISIR-I can be stated as follows.

A ship route is sought departing from $A = (\boldsymbol{x}_A, t_A)$ and arriving at $B = (\boldsymbol{x}_B, t_A + J)$ and minimizing the sailing time J defined by

$$J = \frac{1}{c}\int_A^B n(\boldsymbol{x}, t)\,\mathrm{d}s \tag{1}$$

where $\boldsymbol{x} = [x(t), y(t)]^T$ within an open set $\Omega \subset \mathbb{R}^2$ denotes horizontal position, t is the time variable, and

$$n(\boldsymbol{x}, t) = c/v(\boldsymbol{x}, t)\,, \tag{2}$$

with vessel speed c in calm weather conditions and sustained speed $v(\boldsymbol{x}, t)$ in specific meteo-marine conditions, is the "refractive index" of a horizontal domain of linear extent $\mathrm{d}s$ such that

$$\mathrm{d}s^2 = \mathrm{d}x^2 + \mathrm{d}y^2 \tag{3}$$

Note that the integrand in Eq. (1) can be interpreted as an effective optical depth of the $\mathrm{d}s$ wide domain. The notation is reminiscent of the problem of determining the path

of light moving in a non homogenous medium. Indeed light propagates over paths of stationary optical depth (Fermat's principle).

Ship speed v results from a dynamic balance between forces and torques acting on and from the vessel. This speed is normally found as the solution of differential equations. However, under steady conditions they reduce to algebraic equations of the type:

$$F_{\mathrm{eq}}(\boldsymbol{v};\boldsymbol{p}_{\mathrm{s}},\boldsymbol{p}_{\mathrm{e}}) = 0 \tag{4}$$

where $\boldsymbol{p}_{\mathrm{s}}$ is a set of ship parameters and $\boldsymbol{p}_{\mathrm{e}}$ a set of values of relevant environmental fields evaluated at $(\boldsymbol{x},t)$. Navigational safety also poses limitations on the admissible solutions of Eq. (4). Such limitations are represented as a set of inequalities of the type:

$$F_{\mathrm{ineq}}(\boldsymbol{v};\boldsymbol{p}_{\mathrm{s}},\boldsymbol{p}_{\mathrm{e}}) \leq 0 \tag{5}$$

Parameters $\boldsymbol{p}_{\mathrm{s}}$ and $\boldsymbol{p}_{\mathrm{e}}$ employed in Eqs. (4) and (5) are listed in Table 6.

If the open set Ω is also a connected domain, the existence of a solution to the problem Eqs. (1)–(5) entirely depends on Eqs. (4) and (5): The quality of the route, its topological and nautical characteristics, are determined by these two equations alone.

Speed v resulting from Eqs. (4) and (5) defines the Lagrangian kinematics of the route:

$$\frac{\mathrm{d}s}{\mathrm{d}t} = v(\boldsymbol{x},t) \tag{6}$$

In order to account for uncertainty in the representation of v, a random noise term could be added to the r.h.s. of Eq. (6).

The problem of finding the least-time route in any meteo-marine conditions is thus equivalent to the minimization of J functional with a specified refractive index $n(\boldsymbol{x},t)$, for assigned boundary values A and B.

If the time-dependence in refractive index n is neglected, the general solution of this problem is known from geometrical optics, with routes being refracted towards optically

more transparent regions, according to Snell's law. However, whenever the time scale for changes in the environmental fields is comparable or shorter than the typical route duration, such time-dependence can no longer be neglected and new kinematical features of the least-time route may appear. Indeed, it could be advantageous to wait for some time at the departure location before leaving or voluntarily decrease the speed during navigation, as shown in Sect. 2.2.2 and 2.2.3.

2.2 Shortest path algorithm

The first component of VISIR-I presented here is the shortest path algorithm. The term "shortest path" is used both in the literature and hereafter with a more general sense than a direct reference to the geometrical distance. Indeed, "shortest" may refer to the spatial or temporal distance, as well as the cost or other figure of merit of the optimal path.

2.2.1 Spatial discretization

Let us consider a directed graph $\mathcal{G} = [\mathcal{N}, \mathcal{E}]$. In VISIR-I the nodes $\mathcal{N}$ are part of a rectangular mesh with constant spacing in natural coordinates ($1/60^\circ$ of resolution in both latitude and longitude). As shown in Fig. 1, each node is linked to all its first and second neighbours on the grid, forming the set of edges $\mathcal{E}$. Thus, neglecting border effects, there are 24 connections per node. The specific edge arrangement leads to resolve angles of

$$\theta_{12} = \arctan(1/2) \approx 26.6^\circ \tag{7}$$

Whether such such 24-connectivity should be increased further is questionable, given that the environmental analysis and forecast fields are provided on a coarser grid (by about a factor of 4) than the spatial resolution of the graph, see Sect. 2.4.

In VISIR-I, the resulting graph is first screened for nodes and edges on the landmass. An edge is considered to be on the landmass if at least one of its nodes is on the

landmass or if both nodes are in the sea and the edge linking them intersects the coastline. In such a case, the edge is removed from $\mathcal{E}$, which locally reduces the original 24-connectivity of the graph. When applied to a 1/60° grid for the Mediterranean Sea region (mode 1 of Fig. 8), this procedure still leaves more than 20 million sea edges in $\mathcal{E}$, see Table 2. However, for the actual route computations, just a subset of the whole spatial domain is considered (mode 2 of Fig. 8). This subregion is chosen to be large enough so that a further increase in size does not reduce the total sailing time J. At present, the selection of the subregion shape and extent is left to the user of the model.

2.2.2 Time-dependent approach

Given that environmental conditions change over a time scale comparable with or shorter than the vessel route duration, edge weights cannot be considered as constants. Thus, in order to solve Eqs. (1)–(3), VISIR-I employs a time-dependent algorithm.

With reference to the nomenclature in Table 1, a time-dependent graph $\mathcal{G}(t)$ is fully defined by the sets of nodes, edges, and time-dependent edge weights: $\mathcal{G}(t) = [\mathcal{N}, \mathcal{E}, \mathcal{A}(t)]$.

Edge weight $a_{jk}(\ell)$ between nodes j and k at time step ℓ is defined as

$$a_{jk}(\ell) = \frac{|\boldsymbol{x}_k - \boldsymbol{x}_j|}{v_{jk}(\ell)} \tag{8}$$

where $v_{jk}(\ell)$ is the edge mean ship speed, depending on the average Φ_{jk} of the values of the environmental fields at nodes j and k:

$$\Phi_{jk} = \frac{1}{2}\left(\Phi_j + \Phi_k\right) \tag{9}$$

evaluated at time $t_\ell = t_1 + \delta_t(\ell - 1)$. Here t_1 is departure time and δ_t is the time resolution of the environmental fields. The functional dependence of $v_{jk}(\ell)$ on Φ_{jk} results from the actual model of the vessel, and is derived in Sect. 2.3.

Thus, in VISIR-I, edge weights $a_{jk}(\ell)$ are non-negative quantities with a dimension of time ("edge delays") and are time-dependent. Note that Eq. (8) is the discrete counterpart of Eq. (6), as long as velocity is non null.

There are various methods for computing shortest paths on a graph. For an overview, see Bertsekas (1998) and Bast et al. (2014). A large literature deals with applications for terrestrial networks, see e.g. Zhan and Noon (1998); Zeng and Church (2009); Goldberg and Harrelson (2005).

A key concept in graph methods is the node label, which can be either temporary or permanent. The permanent label X_j of node j is the minimum value of the objective function (e.g. J of Eq. 1) attainable at that node. A temporary label Y_j is any value before the node label is set to its permanent value. When all node labels are set to their permanent value, Bellman's relation holds (Bertsekas, 1998).

Depending on the way node labels are updated, graph algorithms may be classified into label setting or label correcting algorithms. A label setting single-source single-destination algorithm with fixed departure time is used here.

The fact that in VISIR-I destination node is assigned (through $\boldsymbol{x}_B$ in Eq. 1) leads to a possible degeneracy of the problem, with multiple shortest paths between the specified source and destination node. In Yen (1971) an algorithm is presented for finding several simple shortest paths. In VISIR-I it is deemed that, in presence of time-dependent environmental fields, it is unlikely that an alternative route with exactly the same navigation time exists. Thus, just the least-time route is sought after.

In general, the fact that a graph is time-dependent means that the shortest path can have special features. In fact, under specific circumstances, the strategy of traversing an edge as soon as possible does not always lead to the shortest path. Also, the shortest path may not be simple (there may be loops) or even not concatenated (Bellman's optimality not fulfilled). This has consequences on the class of algorithm to be applied. Orda and Rom (1990) show that in this respect the critical condition is how fast edge delays vary in time. If $a_{jk}(t)$ is a differentiable function of time t, the authors show that,

provided

$$\frac{\mathrm{d}}{\mathrm{d}t} a_{jk}(t) \geq -1\,, \tag{10}$$

the best strategy for recovering a shortest path is traversing edge (jk) without waiting at node j (First-In First-Out or: FIFO). Indeed, waiting for a time $\mathrm{d}t > 0$ would in best case be compensated but never overcome by a related decrease $|\mathrm{d}a_{jk}| \leq \mathrm{d}t$ in edge delay. The authors also show that a FIFO time-dependent algorithm has the same computational complexity as a static algorithm.

Typically, condition Eq. (10) may be violated during the decaying phase of a rapidly moving storm. Since VISIR-I employs sea state fields for the Mediterranean Sea, the variability of edge delays is usually low, so that condition Eq. (10) is generally fulfilled, as seen from Fig. 2. The FIFO condition Eq. (10) is also checked at each run of the model and is generally found to be fulfilled. Thus, Dijkstra's static algorithm (Dijkstra, 1959) is modified according to the guidelines of Orda and Rom's FIFO time-dependent algorithm. Related pseudocode is provided in Appendix A.

Before the algorithm is run, edge delays $a_{jk}(\ell)$ are checked for nautical safety constraints, Eq. (5). If at time step $\overline{\ell}$ an edge $(\overline{j}\,\overline{k})$ is unsafe for navigation, we set $a_{\overline{j}\,\overline{k}}(\overline{\ell}) = \infty$. As seen from Fig. 2, this approach generates gaps in $a_{\overline{j}\,\overline{k}}(t)$ as a function of continuous time t. Such gaps are specific time windows during which the edge is not available for linking its nodes. Whenever edges are removed at specific time steps, a FIFO strategy is no longer guaranteed to be optimal, even though edge delays vary slowly. A source-waiting strategy may be necessary in this case (Orda and Rom, 1990). As a consequence, a route retrieved through a FIFO algorithm may still be sub-optimal. This advanced issue is left open for future versions of the system.

2.2.3 Voluntary speed reduction

As seen above, VISIR-I's strategy regarding navigational safety is to remove unsafe edge delays from the graph by setting their edge weight to ∞, prior to the computation

of the optimal route. In addition, as will be shown in Sect. 2.3.3, vessel speed v affects the safety constraints. Thus, a modification of v may help in keeping an otherwise unsafe edge in the graph. This, in turn, may contribute to optimization, since avoiding the removal of elements from set $\mathcal{A}(t)$ can only lower the length of the shortest path. Such voluntary variations in speed should be contrasted with an involuntary speed reduction due to vessel energy loss, caused by interaction with the environmental fields, see Sect. 2.3.2.

VISIR-I defines, for a vessel with maximum engine power $P_{\max}$, a set of possible values $P^{(s)}/P_{\max}$ of engine throttle:

$$P^{(s)} = P_{\max} \cdot g(s) \tag{11}$$
$$s \in [1, N_{\mathrm{s}}]$$

Then, at each edge, speeds $v_{jk}^{(s)}(\ell)$ are computed using the ship model. The function $g(s)$ is chosen in order to linearly space engine throttle values, Table 3 (due to the non-linearity of the vessel model, this choice does not imply linearly spaced values of sustained speed, see Fig. 5). Next, throttle-dependent edge weights $a_{jk}^{(s)}(\ell)$ are computed via Eq. (8). Each of these edge weights is checked to see whether it complies with navigational safety constraints. If an edge is unsafe, its edge weight is set to ∞. Finally, the throttle value s^* leading to the minimum edge weight is chosen by the algorithm:

$$s^* = \underset{s}{\operatorname{argmin}} \left\{ a_{jk}^{(s)}(\ell) \right\} \tag{12}$$

and the edge weight is set to such a minimum value:

$$a_{jk}(\ell) = a_{jk}^{(s^*)}(\ell) \tag{13}$$

Given the ordering in Table 3, if $s^* > 1$ then voluntary speed reduction is useful for recovering a faster route which is still safe with respect to ship stability constraints.

2.3 Ship model

The second component of VISIR-I is a ship model describing vessel interaction with the environment (specified by the forecast fields of Sect. 2.4) and its stability requirements.

The following presentation comprises a balance equation for the propulsion system Sect. 2.3.1, a parametrization of the hull resistance due to calm and rough sea Sect. 2.3.2, and a set of dynamic conditions for the intact stability of the vessel Sect. 2.3.3.

2.3.1 Propulsion

Motorboats are the focus of VISIR-I route optimization.

For these vessels, propulsion is provided by a thermal engine burning fuel and delivering a torque to the shaft line and, when present, to a gearbox. This torque is eventually transmitted to a propeller, converting it into thrust available to counteract resistance to advancement (Journée, 1976; Triantafyllou and Hover, 2003).

A full modelling of this energy conversion mechanism is a highly complex task involving, just to mention a few, the efficiency of each of these conversion steps, the effect of hull-generated wake on propeller efficiency and corresponding thrust deduction, and the load conditions of the engine (MANDieselTurbo, 2011). A quantitative description of these processes requires a detailed knowledge of engine and vessel behaviour. This could be obtained by standard measurement procedures such as those provided by the International Towing Tank Conference (ITTC, 2002, 2011b).

For the purposes of VISIR-I, it was deemed sufficient to derive the vessel response function from a power balance. That is, given the brake power P, the total propulsive efficiency η and the total resistance $\boldsymbol{R}_\mathrm{T}$ *applied to* the vessel, it is required that

$$\eta P = -\boldsymbol{v} \cdot \boldsymbol{R}_\mathrm{T}(v) \tag{14}$$

where $\boldsymbol{v}$ is ship velocity in steady conditions. The l.h.s. of Eq. (14) represents the power available at the propeller, while resistance $\boldsymbol{R}_\mathrm{T}(v)$ depends on both environmental and

ship parameters. One of its possible representations is derived in Sect. 2.3.2. The efficiency η results from the product of several components related, for example, to hull shape, propeller, and shaft characteristics (MANDieselTurbo, 2011). At the present stage of modelling, the value of η is estimated to a constant (see Table 4) and will be refined when a more detailed vessel model is used.

2.3.2 Resistance

In this paper we restrict our attention to displacement vessels. Indeed high speed planing hulls are characterized by a different dynamic behaviour and deserve a more sophisticated treatment (Savitsky and Brown, 1976).

When underway, a displacement vessel is subject to various forces hindering its motion. A possible decomposition of the resulting force is to distinguish calm water resistance $\boldsymbol{R}_\mathrm{c}$ from resistance $\boldsymbol{R}_\mathrm{aw}$ due to only sea waves,

$$\boldsymbol{R}_\mathrm{T} = \boldsymbol{R}_\mathrm{c} + \boldsymbol{R}_\mathrm{aw} \tag{15}$$

Since calm water resistance is always opposite to the ship direction of advance, decomposition Eq. (15) enables Eq. (14) to be rewritten as

$$\eta P = v\,(R_\mathrm{c} + R_\mathrm{aw}\cos\alpha) \tag{16}$$

where α is the angle between wave direction and vessel direction of advance (as seen from Fig. 3, $\alpha = 0$ in case of head waves).

The module of the calm water resistance is usually given in terms of a dimensionless drag coefficient C_T defined by the equation

$$R_\mathrm{c}(v) = C_\mathrm{T}\frac{1}{2}\rho S v^2 \tag{17}$$

where also sea water density ρ and ship wetted surface S appear.

As outlined in ITTC (2011a), C_T depends not just on viscous effects but also on energy dissipated in gravity waves generated by the vessel ("residual resistance"). The latter introduces a dependence on Froude Number Fr which, under Froude's hypothesis, is additive: $C_T(R, Fr) \approx C_F(R) + C_R(Fr)$, where R is Reynold's number and C_R is the residual resistance drag coefficient (Newman, 1977).

In VISIR-I, at this first stage in the development of the ship model, C_T is taken as a constant. This is done in order to easily identify the unknown coefficients in the r.h.s. of Eq. (17). Indeed, the $C_T S$ product is obtained by equating the maximum available power at the propeller to the power dissipation occurring at top speed c in calm water:

$$\eta P_{max} = c \cdot R_c(v = c) = C_T \frac{1}{2} \rho S c^3 \tag{18}$$

The impact of assuming a constant C_T is to overestimate it at low speeds, as this coefficient is identified using the top speed regime, Eq. (18).

In addition to calm water resistance, sea waves are an additional source of ship energy losses (Lloyd, 1998). Various authors have found that wave-added resistance R_{aw} depends on reduced wavenumber L/λ, where L is ship length. Both radiation (energy dissipated due to heave and pitch movements) and diffraction (energy dissipated by the hull to deflect short incoming waves) contribute to this additional resistance. Both effects were modeled by Gerritsma and Beukelman (1972) in head seas, which however are the most severe conditions in terms of added resistance. They found that diffraction increases resistance at $L/\lambda > 1$. In the framework of a comprehensive study of experimental results and several different theoretical methods, Ström-Tejsen et al. (1973) endorsed the method by Gerritsma and Beukelman (1972).

In VISIR-I, a simplified approach for estimating R_{aw} is used. Following the cited literature, a reduced non-dimensional resistance σ_{aw} is introduced:

$$R_{aw} = \sigma_{aw}(L, B, T, Fr) \cdot \frac{\rho g_0 \zeta^2 B^2}{L} \cdot \varphi\left(\frac{\lambda}{L}, \alpha\right) \tag{19}$$

The relation between wave amplitude and significant wave height is $2\zeta = H_s$. In Eq. (19) a factor φ is highlighted, containing the spectral and angular dependencies. This factor is eventually set to a constant value φ_0. This approximation is also done in view of the fact that the full wave spectrum is not used for weighting R_{aw}, as instead done, for example, in Ström-Tejsen et al. (1973). In line with dropping the α dependence in φ, the vectorial nature of $\boldsymbol{R}_{aw}$, Eq. (16), is ignored by assuming that this force is always opposite to the ship's forward speed in a longitudinal direction ($\alpha = 0$).

A simplified method for deriving σ_{aw} when the hull geometry is not available in its entirety was proposed by Alexandersson (2009). We slightly modified his results into:

$$\sigma_{aw} = \widetilde{\sigma_{aw}} Fr / \widetilde{Fr} \tag{20}$$

$$\widetilde{\sigma_{aw}} = 20.(B/L)^{-1.20}(T/L)^{0.62} \tag{21}$$

Further details of this derivation can be found in Appendix B.

Combining Eqs. (20)–(21) with Eq. (19) shows that an increase in either ship beam or draught leads to an increase in resistance, while an increase in length has the opposite effect. This conclusion should be validated through towing tank measurements on the specific hull geometry.

Replacing Eqs. (15)–(21) into Eq. (14) where $\alpha = 0$, the following expression is found to relate ship speed to brake power, geometrical vessel parameters, and environmental fields:

$$k_3 v^3 + k_2 v^2 - P = 0 \tag{22}$$

where the coefficients are given by

$$k_3 = \frac{P_{max}}{c^3} \tag{23}$$

$$k_2 = \widetilde{\sigma_{aw}} \frac{1}{\eta \widetilde{Fr}} \varphi_0 \rho \zeta^2 B^2 \sqrt{g_0 / L^3} \tag{24}$$

Note that Eq. (22) is in the form of Eq. (4) with parameters $\boldsymbol{p}_s$ and $\boldsymbol{p}_e$ as in Table 6.

Sustained speed v is the sole positive root of cubic equation Eq. (22) (in fact, both k_3 and k_2 coefficients are positive quantities). This is computed through an analytical expression whose numerical implementation is provided by Flannery et al. (1992, Sect. 5.6). In Fig. 4 corresponding sustained Froude numbers Fr are displayed. Fr follows a half-bell shaped curve, with a nearly hyperbolical ($\sim 1/H_s$) dependence for large significant wave height. However, in the results shown by Bowditch (2002, Fig. 3703) for a commercial 18-knot vessel, a change of convexity of the Fr curve is not visible, for the H_s range shown. Our results also prove that, by varying engine throttle, sustained speed does not vary by the same factor at all H_s. This result could not be obtained by factorizing the throttle dependence, as in the ship model by Perakis and Papadakis (1989). Furthermore, by comparing performances of vessel V1 (ferryboat) and V2 (fishing vessel) in Fig. 4, it can be seen that the former sustains a larger fraction of its top Froude number at any given significant wave height. This different dynamic behaviour is mainly related to the maximum engine brake power P_{max} of the two vessels. This is found by swapping just P_{max} of the two vessels and keeping unchanged the other parameters provided in Table 5 (not shown).

Figure 5 shows how the throttle needs to be adjusted to sustain a given speed in different sea states. An increase in speed requires an over-proportional increase in throttle. This leads, for each given sea state, to a so called "wave wall" (MANDiesel-Turbo, 2011). Lloyd (1998) makes the assumption that the engine delivers constant power at a given throttle setting, regardless of the increased propeller load due to rough weather (note that propeller load is not considered in VISIR-I either). He then finds that the power required for sustaining a given speed steeply rises with wave height, similar to Fig. 5. The comparison between V1 and V2 also shows that the two vessels behave very differently in extreme seas, whereby vessel V1 (the ferryboat) is able to reach more than 30 % while V2 (the fishing vessel) less than 20 % of its top Fr. Again it is important to note that these results were obtained under the hypothesis of neglecting the residual resistance in C_T.

Resistances are evaluated from the sustained speed v as:

$$R_c = \eta k_3 v^2 \tag{25}$$

$$R_{aw} = \eta k_2 v \tag{26}$$

and corresponding values are shown in Fig. 6.

While calm water resistance R_c does not explicitely depend on significant wave height H_s, R_c depends on ship speed which, through Eqs. (22)–(24), depends on H_s. Thus, assuming maximum throttle, a functional dependence $R_c = R_c(H_s)$ can be computed and is displayed in Fig. 6. Due to the fact that k_3 is independent of H_s (Eq. 23), calm water resistance R_c is dominated by the $v = v(H_s)$ relationship seen in Fig. 4.

Wave added resistance R_{aw} as a function of H_s initially grows quadratically and, for higher waves, only linearly, Fig. 6. This is due to the combined effect of the quadratic dependence on wave amplitude in k_2 (Eq. 24) and the nearly hyperbolic ship speed reduction for large H_s seen in Fig. 4. The same trend is observed in (Lloyd, 1998, Fig. 3.13) and Nabergoj and Prpić-Oršić (2007).

In comparison to V2, vessel V1 exhibits larger resistances. However, for both vessel classes, the R_c and R_{aw} curves form "scissors", being wider for the larger vessel (V1), Fig. 6.

2.3.3 Stability

The ship model described so far needs to be complemented by navigational constraints in order to reduce dangerous or unpleasant movements for the ship itself, the crew and cargo.

Such situations cannot simply be ruled out by designing a vessel in accordance with the Intact Stability (IS) Code, IMO (2008). In fact, specific combinations of meteorological and sea-state parameters may lead to dangerous situations even for ships complying with such mandatory regulations (Umeda, 1999; IMO, 2007). Furthermore, in Belenky et al. (2011) the point is made that new ship forms can make the prescription

of the IS code obsolete. This led to the development of "second generation" stability criteria, being more physics and less statistics based than IS criteria.

VISIR-I checks for three modes of stability failure: parametric roll, pure loss of stability, and surfriding/broaching-to. The theoretical hints below are mainly based on Belenky et al. (2011), while the implementation of the stability checks follows the operational guidance by IMO more closely (IMO, 2007). In view of the limited angular resolution of the graph (Sect. 2.2.1), in VISIR-I stability in turning (Biran and Pulido, 2013) cannot be taken into consideration, and an unlimited vessel manoeuvrability (IMO, 2002) has to be assumed.

A realistic assessment of stability failure would require a detailed knowledge of ship hull geometry. In the present version of VISIR-I, however, just principal particulars of the vessel (length, beam, draught) are employed. In addition, even vessel-internal motions and mass displacements, such as the positioning of catch (Gudmundsson, 2009) and fuel sloshing (Richardson et al., 2005) may have an amplifying effect on the loss of stability. Thus, the bare application of safety constraints described in the following cannot guarantee navigation safety, and the ship-master should critically evaluate the resulting route computed by VISIR-I, also taking account the meteo-marine conditions actually met during the voyage and the specific vessel response.

In the following sections, we have used the deep water approximation in order to gain a rapid estimation of the threshold conditions. We can thus estimate the wavelength as:

$$\lambda[\mathrm{m}] = \frac{g_0}{2\pi} T_\mathrm{w}^2 \approx 1.56\,(T_\mathrm{w}[\mathrm{s}])^2 \tag{27}$$

and the wave phase speed or celerity as:

$$c_\mathrm{p}[\mathrm{kt}] = \sqrt{\frac{g_0 \lambda}{2\pi}} \approx 2.4\,\sqrt{\lambda[\mathrm{m}]} \approx 3 T_\mathrm{w}[\mathrm{s}] \tag{28}$$

Then, assuming a fully developed sea (Pierson–Moskowitz spectrum), the wave steepness can be estimated as:

$$H_\mathrm{s}/\lambda = \frac{2\pi}{g_0}\frac{H_\mathrm{s}}{T_\mathrm{w}^2} = \frac{8\pi}{(24.17)^2} \approx 1/23 \tag{29}$$

This result can be inferred from the plot of characteristic seas reported by Ström-Tejsen et al. (1973). For partially developed seas the wave steepness is larger and for dying seas smaller than the value obtained in Eq. (29).

2.3.4 Parametric roll

When a ship is sailing in waves, the submerged part of the hull changes in time. For most hull shapes, this also involves a change in the waterplane area. This in turn influences the curve for the righting lever (GZ), which is fundamental to ship stability. Indeed, if wavelength λ is comparable to ship length L and waves are met at a specific frequency, the change in GZ may trigger a resonance mechanism, leading to a dramatic amplification of roll motion (Belenky et al., 2011). A famous naval casualty ascribed to this mechanism of stability loss is reported in France et al. (2003).

The mathematical formulation of parametric roll is based on the solution of Mathieu's equations and the computation of Ince–Strutt's diagram. It shows that parametric roll occurs when encounter wave period T_E satisfies the condition

$$2T_\mathrm{E} = \pm n T_\mathrm{R}, n = 1, 2, 3, \ldots \tag{30}$$

where T_R is the ship's natural roll period (Spyrou, 2005) and the ± sign in Eq. (30) accounts for both following and head seas.

In VISIR-I the encounter period T_E is obtained by applying a Doppler's shift to peak wave period T_w and reads

$$T_\mathrm{E} = T_\mathrm{w} \cdot \left[1 + \frac{v \cos\alpha}{3 T_\mathrm{w} K(T_\mathrm{w}, z)}\right]^{-1} \tag{31}$$

where Fenton's factor K defined by Eq. (48) is used (v in kt). Instead, IMO's formula for T_E provided in (IMO, 2007, 1.6) corresponds to the deep water approximation, i.e. to the case $K = 1$. Since in shallow waters and large wave periods $K < 1$, IMO's formula may lead to an overestimation of T_E.

Levadou and Gaillarde (2003) observe that a smaller GM also implies a larger natural roll period T_R and thus a parametric roll experienced in presence of longer waves. Spyrou (2005) points out that, while any encounter angle α can in principle lead to parametric roll, vessels with low metacentric height GM (and, thus, large T_R) may be more prone to experience parametric roll during following than head seas (due to larger $|T_E|$).

Following (Levadou and Gaillarde, 2003) and the wave height criterion reported for $L < 100$ m in Belenky et al. (2011), the parametric roll hazard condition is implemented in VISIR-I as:

$$0.8 \leq \lambda/L \leq 2 \tag{32}$$

$$H_s/L \geq 1/20 \tag{33}$$

together with Eq. (30) expressed in the form of the inequalities:

$$1.8|T_E| \leq T_R \leq 2.1|T_E| \tag{34}$$

$$0.8|T_E| \leq T_R \leq 1.1|T_E| \tag{35}$$

where the coefficients in Eqs. (34)–(35) should be related to the roll damping characteristics of the vessel (Francescutto and Contento, 1999), but for the current version of VISIR-I they are taken from Benedict et al. (2006).

Formula Eq. (31) shows that T_E period may be tuned by varying the speed and course of the vessel. Thus, to prevent parametric rolling, a routing algorithm may suggest either a voluntary speed reduction or a route diversion. As shown in Sect. 2.2.3 and as will be seen in the case studies (Sect. 3), VISIR-I is able to exploit either option.

2.3.5 Pure loss of stability

This mode of stability failure is triggered by a similar condition to the parametric roll. However, it does not involve any resonance mechanism and thus may be activated by a single wave. In fact, if the crest of a large wave is near the midship section of the ship, stability may be significantly decreased. If this condition lasts long enough (such as during following waves and ship speed close to wave celerity), the ship may develop a large heel angle, or even capsize.

According to Belenky et al. (2011) a useful criterion for distinguishing ships prone to pure loss of stability involves a detailed knowledge of hull geometry. The IMO guidance (IMO, 2007) however proposes using just ship-wave kinematics. This is also the criterion adopted in VISIR-I and can be stated as the following conditions to be simultaneously verified:

$$\lambda/L \geq 0.8 \tag{36}$$

$$H_s/L \geq 1/25 \tag{37}$$

$$|\pi - \alpha| \leq \pi/4 \tag{38}$$

$$1.3T_w \leq v \cdot \cos(\pi - \alpha) \leq 2.0T_w \tag{39}$$

where ship speed v is given in kt.

Using also Eqs. (27)–(28) it can be seen that Eq. (39) implies (for exactly following seas) a sustained speed v between 43 and 67 % of wave celerity c_p.

2.3.6 Surfriding/broaching-to

Surfriding is the condition where the wave profile does not vary relative to the ship. That is, the ship moves with a speed equal to wave celerity: $v = c_p$. In this case, the ship is directionally unstable, with the possibility of an uncontrollable turn known as "broaching-to".

The simplest modelling of this mode of stability failure starts with the computation of the force of the wave-induced surge which is able to balance the difference between total resistance and thrust provided by the ship. A critical point may then be reached, where surging is no longer possible and the ship is captured by the surfriding mode (Belenky et al., 2011). This phase transition is a heteroclinic bifurcation (Umeda, 1999).

In IMO (2007) a surfriding condition is proposed which just takes into account ship speed and length, independently of wave steepness. Based on numerical simulations, Belenky et al. (2011) overcomes this simplification, with the finding that the phase transition is less likely for less steep waves.

In VISIR-I, the following surfriding hazard criteria reported in Belenky et al. (2011) are considered:

$$0.8 \leq \lambda/L \leq 2 \tag{40}$$

$$H_s/\lambda \geq 1/40 \tag{41}$$

$$|\pi - \alpha| \leq \pi/4 \tag{42}$$

$$Fr \cdot \cos(\pi - \alpha) \geq Fr_{crit} \tag{43}$$

where the critical Froude number is given by

$$Fr_{crit} = 0.2324(H_s/\lambda)^{-1/3} - 0.0764(H_s/\lambda)^{-1/2} \tag{44}$$

Using Eq. (29) its typical value is found to be $Fr_{crit} = 0.31$. Condition Eq. (41) was added to VISIR-I since Fr_{crit} is reported in Belenky et al. (2011) just for the range $Fr \in [1/40, 1/8]$. Condition Eq. (43) was complemented with an α dependence in analogy with Eq. (39) in order to account for following-quartering seas. This implies that surfriding is less likely to occur for quartering than following seas, since Fr is multiplied by a factor which may be as small as $1/\sqrt{2}$.

Of note is that all VISIR-I safety constraints described above, Eqs. (32)–(43), are implemented in negative, i.e., as the set of conditions possibly leading to a stability loss. Nevertheless, they are all still in the form of Eq. (5) with parameters $\boldsymbol{p}_s$ and $\boldsymbol{p}_e$ as in Table 6.

2.4 Environmental fields

We distinguish the environmental fields between static (bathymetry and coastline) and dynamic fields (waves, winds, currents). In VISIR-I, bathymetry and coastline are employed to ensure that navigation occurs in not too shallow waters and far from obstructions. Of the dynamic fields, just wave forecast fields are used, as explained below.

2.4.1 Static fields

A $1/60^\circ$ (= 1 Nautical Mile or 1 NM) bathymetry is used in VISIR-I. The dataset (NOAA Digital Bathymetric Data Base[3]) is used for a twofold purpose: (i) Along with the coastline database, bathymetry is needed for computing a land–sea mask for safe navigation. The first step is to select edges (jk) satisfying the condition that edge averaged sea depth $z = (z_j + z_k)/2$ is larger than ship draught T:

$$z > T \tag{45}$$

In other words, for navigation just a strictly positive Under Keel Clearance UKC $= z - T$ is admitted. (ii) Bathymetry is also needed for a more accurate estimation of wavelength λ, which is an important quantity for vessel stability checks of Sect. 2.3.3. Indeed deep water approximation tends to overestimate λ in shallow waters. Instead, VISIR-I employs Fenton's approximation (Fenton and McKee, 1990) which, upon the introduction of the deep water limit λ_0 for wavelength of the component of peak period T_w,

$$\lambda_0 = \frac{g_0}{2\pi} T_w^2 \tag{46}$$

[3] http://www.ngdc.noaa.gov/mgg/bathymetry/iho.html

can be rewritten as follows:

$$\lambda = \lambda_0 \cdot K(T_w, z) \tag{47}$$

$$K(T_w, z) = \left\{ \tanh \left[\left(\frac{2\pi z}{\lambda_0} \right)^{3/4} \right] \right\}^{2/3} \tag{48}$$

As seen from Eq. (48), in order λ to sense the effect of shallow water, z should be small with respect to the scale set by λ_0.

The coastline database is used in VISIR-I for a preliminary removal of the graph edge on the landmass (Sect. 2.2.1) and, jointly with the bathymetry, for the computation of a nautically safe land–sea mask (see below).

To this end, the NOAA Global Self-consistent, Hierarchical, High-resolution Geography Database (GSHHG[4]) is employed. Just two hierarchical levels are considered: the coastline of the Mediterranean basin and its islands. The minimum distance between coastline data points is variable and is in some cases below 100 m.

A joint depth-coast land–sea mask is obtained by multiplying the mask defined by Eq. (45) with a mask of offshore grid points. Due to the quite different spatial resolution of the coastline and the environmental fields, a regridding procedure is employed for reconstructing the coastal fields:

1. Fields are extrapolated inshore by replacing missing values of sea fields with the average of the first neighbouring grid points, Fig. 7. This "sea-over-land" procedure is distinguished by the extrapolation used in De Dominicis et al. (2013) by: the number of neighbours used (8 and not just 4) and the absence of the condition that at least two neighbouring grid points have assigned field values. Sea-over-land can be iterated in order to define field values on further neighbouring land grid points.

[4] http://www.ngdc.noaa.gov/mgg/shorelines/gshhs.html

2. The fields are bi-linearly interpolated to the target grid. In VISIR-I this is the bathymetry grid. Thus, spatial resolution of wave fields is enhanced from the original 1/16 to 1/60°.

2.4.2 Dynamic fields

The dynamic environmental fields are used in VISIR-I for the computation of sustained ship speeds and safety constraints. In the present version, just the effect of waves is considered, which is deemed to be the most relevant for medium and small-size vessels. The effect of wind and sea currents is planned for future development:

1. Wind drag may be significant for vessels with a large freeboard and/or superstructure area (Hackett et al., 2006);

2. Sea current drift is relevant especially in proximity to strong ocean currents (Takashima et al., 2009) and for not too fast vessels with large draughts;

3. Wave effects include both drift and involuntary speed reduction. The drift is due to nonlinear mass transport in waves (Stokes'drift, Newman, 1977). It is small when the reduced wavenumber L/λ is smaller than unity and increases significantly when $L/\lambda \approx 1$ (Hackett et al., 2006). Involuntary speed reduction in waves was instead detailed in Sect. 2.3.

Thus, the effect of wind drag may be neglected for not too large vessels, and the effect of current and wave drift for vessels able to sustain significantly larger speeds than the current magnitude. In addition, since coastal wave fields may be affected by the extrapolation/interpolation procedure, and due to the current resolution of the bathymetry grid (1 NM) (Sect. 2.4.1), also very small vessels, sailing coastwise on short routes, should be removed from the scope of this system. Thus, we roughly estimate the range of admissible vessel lengths L to be up to a few tens of meters.

The current version of VISIR-I employs wave forecast fields from an operational implementation of Wave Watch III (WW3) model (Tolman, 2009) in the Mediterranean

Sea, delivered by INGV (Istituto Nazionale di Geofisica e Vulcanologia) as a part of the Mediterranean Ocean Forecasting System (MFS) system. WW3 is a spectral model that considers (for deep water conditions) the following as action source and sink terms: wind forcing, whitecapping dissipation, and nonlinear resonant wave-wave interactions. Details on the physical mechanisms implemented in the current application in the Mediterranean Sea can be found in Clementi et al. (2013). The wave model is coupled to the hydrodynamics forecasting model NEMO, part of the Copernicus Marine Service: Pinardi and Coppini (2010), Oddo et al. (2014), and Tonani et al. (2014, 2015). The coupling involves an hourly exchange of sea surface temperature, sea surface currents, and wind drag coefficients between the two models (Clementi et al., 2013). The WW3 model is horizontally discretized on a $1/16^\circ$ mesh. Wind forcing is through $1/4^\circ$[5] resolution ECMWF model forecast fields with 3 hourly resolution for the first three days and then a 6 hourly resolution. For the case studies of Sect. 3, fields from WW3 run in hindcast mode are employed: ECMWF analysis are used as a forcing for both the wave and the hydrodynamic model and NEMO is run in data assimilation mode. The spectral discretization of the current WW3 implementation is: 24 equally distributed angular bins (i.e. 15°) and 30 frequency bins ranging from 0.05 Hz (corresponding to a period of 20 s) to 0.79 Hz (corresponding to a period of about 1.25 s). The operational product used in input by VISIR-I, however, does not employ the full spectral dependence, but just the peak wave period T_w, significant wave height H_s and wave direction θ_w. Hourly output fields of the MFS-WW3 model are employed by VISIR-I.

2.5 Outline of the computational implementation

Here we present the main steps in the computational implementation of VISIR-I into a computer code. The code itself can be obtained following the instructions provided in Appendix C.

[5] $1/8^\circ$ for the operational version of VISIR-I.

The flow chart in Fig. 8 shows that there are two distinct VISIR-I functioning modes. In both modes, the first step is to prepare the model grid for creating graph nodes and edges.

Mode 1 is needed to produce the database of nodes and edges neither lying on the landmass nor crossing it, see Table 2. Sea nodes are computed first, since sea edges are a subset of the edges linking sea nodes (an edge can link sea nodes and still cross the landmass). This selection is a time-consuming process and at the same time completely independent of the forecast fields. Thus, mode 1 is run once and for all for a given topology of the domain (coastline) and graph structure (grid resolution and connectivity). The resulting database of nodes and edges is then employed as VISIR-I runs in mode 2.

Mode 2 is the functioning mode for the operational use of VISIR-I. First of all, the ship model is evaluated. Equation (22) is solved and a Look-Up Table of ship speed values $v = v(P^{(s)}, H_\mathrm{s})$ as a function of engine power settings $P^{(s)}$ and significant wave heights H_s is prepared, as described in Sect. 2.3.2. All environmental fields are then subset to the domain where the route is to be searched. Gridded fields are converted to edge average quantities through Eq. (9). In order to compute the time-dependent edge weights $a_{jk}(\ell)$, the Look-Up Table $v = v(P^{(s)}, H_\mathrm{s})$ is linearly interpolated to the actual H_s value relative to each edge. At the same time, edge weights of set $\mathcal{A}(t)$ that at specific times t are not compliant with the navigational safety constraints are set to ∞. The shortest path algorithm is then run twice. First, it is run in its time-independent version using the geodetic distance between nodes as edge weight[6]:

$$a_{jk} = |\boldsymbol{x}_k - \boldsymbol{x}_j| \tag{49}$$

This computes a still safe geodetic route from a topological viewpoint (coastline and bathymetry already checked at previous steps). The time-dependent shortest path algorithm is then run with time-dependent edge weights $a_{jk}(\ell)$ from Eq. (8). The output

[6] Such weights, like those in Eq. (8), are still nonnegative quantities. However, unlike Eq. (8), they have dimensions of length and not time.

of the shortest path algorithm is a set of nodes and times at which they are visited. This information is necessary and sufficient for reconstructing all environmental fields ($H_s, \theta_w, T_w, T_E, z$) and ship status variables ($\boldsymbol{x}$, $P, v, \hat{v}$) along the route.

In VISIR-I, for long routes, the computing time is dominated by the shortest path computation. The performance of the shortest path routine depends on whether it is run for the computation of the geodetic route (thus using static edge weights, Eq. 49) or for the optimal route (time-dependent edge weights, Eq. 8). However, in line with the theoretical performance of Dijkstra's algorithm (Dijkstra, 1959), the computing time τ is in both cases quadratic in terms of the number N of gridpoints included in the selected spatial domain for the route computation:

$$\tau = c_0 + c_1 N + c_2 N^2 \tag{50}$$

with coefficients as in Table 9. As can be seen, the optimal route asymptotically requires a computing time less than 3 % longer than the geodetic route. The performance Eq. (50) could be improved by making use of data structures such as binary heaps (Bertsekas, 1998).

2.6 Validation

An exact validation of the optimization algorithm of VISIR-I and the forthcoming post-processing phase is possible in the case of time-invariant fields. However, algorithmic complexity and pseudocode do not substantially differ for the case of time-invariant and time-dependent fields, as pointed out in Sect. 2.2.2. In fact, they basically differ just in using edge weight $a_{jk}(\ell)$ instead of a_{jk} in row #9 of pseudocode in Appendix A. Thus, a validation of the algorithm for time-invariant fields covers a more general scope.

We thus exploit the cycloidal curve, being the solution to problem Eqs. (1)–(3) if speed v is proportional to the square root of one of the horizontal coordinates. If speed

is given by $v = \sqrt{2g(2\mathcal{R} - y)}$ the solution is an inverted cycloid:

$$x(y) = \mathcal{R} \cdot \arccos\left(\frac{y}{\mathcal{R}} - 1\right) - \sqrt{y(2\mathcal{R} - y)} \tag{51}$$

$$0 \le x \le \pi\mathcal{R} \tag{52}$$

where $2\mathcal{R}$ is the distance between departure and arrival point along y direction and $0 \le y \le 2\mathcal{R}$ (Lawrence, 1972). Thus, the aspect-ratio of the cycloid is defined solely by parameter $\mathcal{R}$. On the other hand, time J for moving between the two endpoints of the curve under the influence of a "gravity force" also depends on g parameter, see formulas in Table 10.

Figure 9 proves that the VISIR-I optimal route follows the analytical trajectory of Eq. (51). The geometrical differences are due to the connectivity of the graph, leading to an angular resolution θ_{12}, Eq. (7). In Mannarini et al. (2013), the effect was quantified of graph connectivity on the representation of analytical routes in the absences of environmental fields. In terms of navigation time, the VISIR-I optimal route is also quite accurate with respect to the cycloid, see Table 10. While the length error is about 2 %, the error in sailing time is only 1 %. This is because larger misfits with respect to the cycloidal route are found in the lower latitude portion of the route, where the advance speed is highest and thus a relatively shorter time is spent, and this leads to a smaller accumulation of temporal errors.

Note that the cycloidal profile is compatible with Snell's law of refraction, as the route is refracted in order to reach the optically more transparent (higher speed) region the soonest. Instead, the rhumb line connecting departure and arrival points does not sufficiently exploit such a high speed region and lags behind by more than 18 %, see Table 10.

3 Mediterranean Sea case studies

In VISIR-I, the choice of the vessel parameters (Table 5), the variety of possible sea-states, and the freedom to select departure and arrival from any two points in the Mediterranean Sea give rise to a considerable number of route features. In this section we generate a few prototypical situations, demonstrating the features of the model presented in Sect. 2. As mentioned in Sect. 2.4.2, analysis rather than forecast fields are used for computing the results shown in this section. The FIFO condition of Eq. (10) is checked at each time step of the analysis fields. It turns out that FIFO is always fulfilled in the cases considered.

3.1 Case study #1

In this case study, vessel V1 of Table 5 (a small ferry boat) is operated on the route from Trapani (Italy) to Tunis (Tunisia) during the passage of an intense low system called "Christmas Storm", affecting western Europe on 23–27 December 2013[7]. Several ferry crossings were disrupted or even canceled during this period. Thus, this situation represents a good test-bed for evaluating the effect of extreme sea-state on the route of a medium size vessel.

In Fig. 10 a selection of snapshots between departure and arrival time is shown. The progress of both the geodetic and the optimal route up to the time of the actual snapshot are displayed. After the geodetic route correctly skips the Egadi Islands west of the departure harbour, it sails straight towards its destination. The optimal route instead passes south of the island of Favignana (37.9° N, 12.3° E) and diverts further southwards while crossing the Strait of Sicily. Finally, after a course change towards starboard, it reaches Tunis. This occurs at a time when an identical vessel on the geodetic route and same departure time has not yet reached its destination.

[7] http://www.metoffice.gov.uk/climate/uk/interesting/2013-decwind

Considering the motion of the wave height field as well, the optimal route attempts to maximize the time spent in calmer seas, where, due to the smaller added wave resistance (Eq. 19), the sustained speed is higher. This is why, though longer in terms of sailed miles, the optimal route is significantly faster than the geodetic route, Table 11.

Figure 11 further analyses the temporal evolution of the two routes. Beginning about $\Delta t = 6$ h after departure, a saw-tooth feature in the time history of H_s and v variables is displayed. This is due to the temporal variation of the wave field, which is fast on the scale of the time step duration ($\delta_t = 1$ h) at which the analysis fields are provided. However, we checked that the FIFO condition of Eq. (10) is still satisfied for this route. Superimposed on the saw-tooth, there are smaller steps in both H_s and v timeseries, roughly any $\delta_g = \delta x / v \sim 0.1$ h, where $\delta x = 1$ NM is the horizontal grid spacing and $v \approx 10$ kt is the ship speed at $\Delta t = 6$ h. These smaller steps are due to the strong spatial gradients of the local significant wave height field. The encounter wave period panel shows that, at about $\Delta t = 12$ h, T_E of the optimal route nearly matches T_R. This is one of the necessary conditions for parametric rolling, as required by Eq. (35). However, the panel with the danger indexes shows that such danger conditions are not activated. This is due to a large wavelength $\lambda > 2L$, non matching criterion Eq. (32).

3.2 Case study #2

In the second case study, a transfer of fishing vessel V2 of Table 5 between the islands of Crete and Rhodes (Greece) is assumed to occur during a Meltemi (north wind) situation, typical for the Aegean Sea.

In Fig. 12 the geodetic and optimal routes are displayed on top of the wavelength field. In this case, wavelength λ is often comparable to vessel length, as clearly seen from the λ time history in Fig. 13. This condition favours, along the geodetic route, the infringement of the stability criteria for both parametric roll and pure loss of stability of Sect. 2.3.3. In fact, the reduced wavelength λ/L controls the activation of all safety constraints (see Eqs. 32, 36, and 40). However, this is not the reason for the diversion south of island of Karpathos (35.4° N, 27.2° E) suggested by VISIR-I, which is

still driven by the refraction effect through calmer seas (this can be seen by switching off the check on the safety constraints). Both routes correctly avoid all obstructions, maintaining a positive UKC, as required by Eq. (45). Finally, we note that for such an "archipelagic" domain and large T_w, shallow waters significantly affect wave dispersion. For example, the wavelength λ during the first hour of navigation would be overestimated by about 20 % if, in place of Fenton's approximation Eqs. (47)–(48), the deep water approximation were employed in a region where $z < 50$ m (not shown).

3.3 Case study #3

In the third case study, a voyage of fishing vessel V2 of Table 5 from Gibraltar (UK) to Sidi Ali (Algeria) is simulated during a wave event past the strait of Gibraltar into the Mediterranean Sea.

Figure 14 shows a northbound diversion of the optimal route compared to the geodetic route, being instead along a line of constant latitude. The diversion results in the optimal route reaching the destination significantly later than the geodetic route, see Table 11. However, this is still compliant with the least-time objective of VISIR-I, as in this case the northbound diversion is forced by the safety checks (as proven from Fig. 14e, where they are disabled). Both pure loss of stability and surfriding may occur along the geodetic route, as seen from Fig. 15. This is due to prevailing following seas and short wavelength, comparable to vessel length. Parametric roll instead is inhibited due to large $|T_E|$, resulting from fetch, Fig. 15b. Also, the relatively small significant wave height leads to a sufficiently high sustained speed for the threshold condition on the Froude number Eq. (43) to be overcome, thereby creating surfriding conditions for part of the geodetic route, Fig. 15f. This is one of the reasons why for this route the voluntary speed reduction of Eq. (12) is also at work. As seen from Fig. 15e, the algorithm suggests reducing the throttle to 85 % or 70 % (i.e., $s = 2$ and $s = 3$ of Table 3) for a total of several hours, starting from $\Delta t \approx 13$ h. This reduces the sustained speed (Fig. 15c), enabling the vessel to sail with following seas ($145 \leq |\alpha| \leq 174$) without being exposed to surfriding. According to Fig. 15e, engine throttle is reduced and restored again six

times in the course of about 10 h. The resulting effect on fuel consumption and onboard comfort is neglected by VISIR-I, as the sole optimization objective is the total time of navigation. Indeed, as seen from Table 11, throttle reduction results in a 20 min faster route than with throttle always kept at 100 %. In the latter case, a southbound diversion is also needed in the last part of the route, as seen from Fig. 14f. Finally, as can be seen in Fig. 11, fields along the route exhibit a saw-tooth feature after $\Delta t = 10$ h, due to the rapidly evolving wave field. However, the FIFO condition of Eq. (10) is still satisfied.

4 Conclusions

In this paper, we have presented the scientific basis of VISIR-I, a ship routing system, as well as results of its computation of optimal routes in the Mediterranean Sea. The system is designed for flexible modelling of the vessel and its interaction with the environment. Time-dependent analysis and forecast fields from oceanographic models are employed in input.

The optimal routes computed by VISIR-I were shown to correctly avoid islands and waters shallower than ship draught. Vessel course is generally refracted towards regions of larger sustained speed, allowing in some cases to sail a longer path and reach the destination earlier than along the rhumb line. VISIR-I optimal routes are checked for vessel intact stability, in terms of compliance with IMO regulations and more advanced research results. In some cases, it is these safety criteria, and not the refraction, being responsible for route diversions. The algorithm is also able to compute voluntary speed reductions. The vessel parameters needed to run the model are limited to basic propulsion data and hull principal particulars, making the system accessible for on-demand computations even by non-professionals of navigation.

Several issues require further improvements. In relation to the time-dependent algorithm, in the case of rapid changes in the analysis or forecast fields, the optimality of the route retrieved by the model is no longer guaranteed (see FIFO condition in Sect. 2.2.2). This however is not the case in all the examples provided. In general, the

optimal departure time may include a waiting time, which is not handled by the current scheme. Furthermore, the discretization of the dynamic fields may lead to saw-tooth oscillations in the time history of optimal speed, as seen in Figs. 11 and 15. In some cases, the limited angular resolution of the model and the form of the safety constraints may lead to sudden course changes in the optimal route. For more affordable computations, the graph grid may need a redesigning, thus reducing the density of gridpoints in open seas through the use of a nonuniform mesh. An unstructured (Shewchuk, 2002) or adaptive refinement mesh (Berger and Colella, 1989) could be considered.

For the environmental fields, the most urgent upgrade seems to be to account for wind, especially for larger vessels, and for currents, at least for slower boats. Wind was recently added to a variant of VISIR-I for sailboat routing (Mannarini et al., 2015). Coastal models and limited area weather models could provide the high spatial resolution required for more realistic computations.

Concerning the ship model, a more advanced parametrization of both calm water and wave added resistance (Sect. 2.3) could be devised, e.g. by employing data measured in a towing tank. The dependence of wave added resistance on vessel speed, as well as the vectorial nature and spectral dependence of the total resistance could be considered. Engine modelling could be refined by introducing engine torque and the number of revolutions as well as propeller parameters. A more realistic ship model would also allow for more sensitive optimization objectives, such as onboard comfort, related to the vertical acceleration of the ship.

A summary of the main approximations employed in VISIR-I is provided in Table 7. The first operational implementation of the system took place in the Mediterranean Sea and can be accessed from the webpage http://www.visir-nav.com and the mobile apps linked there.

In the future, VISIR could be generalized to other optimization objectives, such as bunker savings, by suitably modifying the refractive index in Eq. (2). Another interesting upgrade could be to account for the stochastic nature of the environmental fields. For

the vessel modelling, an extension to planing hulls is possible (Savitsky and Brown, 1976).

However, further significant developments of VISIR should be selected and validated in the light of observed data on actual route and vessel dynamics, stemming either from on-board measurements or naval simulators.

Appendix A: Pseudocode of the time-dependent graph method

Here we provide the pseudocode for the time-dependent shorthest path algorithm employed in VISIR-I (see Sect. 2.2.2).

It is organized into three main parts: initialization of node labels and indexes (rows 2–6); main iteration loop (rows 7–10 and 13–17); exit condition (rows 11–12).

The input arguments are the start and end nodes j_s and j_e, the set of graph edges $\{(jk)\}$, and the set of time-dependent edge weights $\{a_{jk}(\ell)\}$. Index f_k in rows 3, 4, 10 represents the predecessor ("father") of node k along the shortest path. δ_t is the time step. The temporary and the permanent label of node j are respectively Y_j and X_j. Row 6 implements the FIFO hypothesis by requiring edge weights to be evaluated at the first available time step ℓ of the environmental fields, as explained in Sect. 2.2.2. In order to speed up access to the set of neighbours of a given node in row 8, a forward star representation of the graph is employed (Ahuja et al., 1988). The minimum label search in row 15 is a typical feature of any Dijkstra's method.

Algorithm 1 DIJKSTRA-TIME

Function DIJKSTRA-TIME (j_s, j_e, $\{(jk)\}$, $\{a_{jk}(\ell)\}$)
Initialization:
$X_s \leftarrow t_1, f_s \leftarrow$ NIL
$\forall k \neq s \quad Y_k \leftarrow \infty, X_k \leftarrow$ NULL, $f_k \leftarrow$ NIL
$j \leftarrow j_s$
$\ell \leftarrow 1 + \text{floor}(X_j/\delta_t)$
Main iteration – part I:
For all neighbours k of j for which X_k = NULL **Do:**
a.) $Y_k \leftarrow \min\{Y_k, X_j + a_{jk}(\ell)\}$
b.) **If** Y_k changed in step a.), **then set** $f_k \leftarrow j$.
Exit condition:
If j_e has non null X value **then stop**.
Main iteration – part II:
Otherwise find the node l such that:
$Y_l = \min_{k \in V} Y_k, \quad V = \{k : X_k = \text{NULL}\}$
Set $X_l \leftarrow Y_l, j \leftarrow l$
Proceed with *Main iteration – part I*

Appendix B: Non-dimensional added wave resistance

The steps leading to the expressions Eqs. (20)–(21) for the non-dimensional added wave resistance σ_{aw} are described in the following.

We start from (Alexandersson, 2009, Eq. 7.11) results. The factor containing the prismatic coefficient is neglected, since its exponent is very close to zero. Also, the longitudinal position of the center of gravity is assumed to be $L/2$ and the pitch radius

of gyration to be $L/4$. The original power law dependence $\sigma_{aw} \sim Fr^{0.64}$ is also replaced by a linear dependence, Eq. (20). This is done to retrieve an analytical solution for ship speed v, see Eq. (22). In order to obtain such linear dependence, a least square fit of $\sigma_{aw} \sim Fr^{0.64}$ is forced through the origin over the domain

$$Fr \in [0, c/\sqrt{g_0 L}] \tag{B1}$$

of the independent variable. The range Eq. (B1) of Fr represents the operational regime of the vessel. The slope $1/\widetilde{Fr}$ of the fitted function identifies the reference Froude number $\widetilde{Fr}$.

Code availability

During the refereeing process, the VISIR-I code is made available through the Editor of GMD to the anonymous referees, for the purpose of the reviewing, under the GNU Lesser General Public License (Version 3, 29 June 2007). Upon publication on GMD, the code will be made available on a public-access resource. The VISIR-I code is written in Matlab and can be run on any workstation or laptop. The currently supported architecture is *nix (tested on Mac OS-X 10.9.5 and Linux CentOS 6.2). Required third party software are the MEXCDF libraries.

Acknowledgements. Funding through TESSA (PON01_02823/2) and IONIO (Subsidy Contract No. I1.22.05) projects is gratefully acknowledged. Pinardi was partially funded by the AtlantOS project (EC H-2020 grant agreement No. 63321).

References

Ahuja, R. K., Magnanti, T. L., and Orlin, J. B.: Network Flows, Tech. Rep., Massachusetts Institute of Technology, 1988. 7948

Alexandersson, M.: A study of methods to predict added resistance in waves, Master's thesis, KTH Centre for Naval Architecture, 2009. 7928, 7949

Bast, H., Delling, D., Goldberg, A., Mueller-Hannemann, M., Pajor, T., Sanders, P., Wagner, D., and Werneck, R. F.: Route Planning in Transportation Networks, Tech. Rep., Microsoft Research, Microsoft Corporation, 2014. 7922

Belenky, V., Bassler, C. G., and Spyrou, K. J.: Development of Second Generation Intact Stability Criteria, Tech. Rep., DTIC Document, 2011. 7930, 7931, 7932, 7933, 7934, 7935

Benedict, K., Baldauf, M., and Kirchhoff, M.: Estimating potential danger of roll resonance for ship operation, in: Schiffahrtskolleg Rostock 2004, Proceedings, vol. 5, 67–93, 2004. 7960

Benedict, K., Baldauf, M. K. M., and Kirchhoff, M.: Decision support for avoiding roll resonance and wave impact for ship operation in heavy seas, in: Safety and Reliability for Managing Risk, edited by: Zio, G. S., 2743–2750, 2006. 7933

Berger, M. J. and Colella, P.: Local adaptive mesh refinement for shock hydrodynamics, J. Comput. Phys., 82, 64–84, 1989. 7947

Bertsekas, D.: Network Optimization: Continuous and Discrete Models, Athena Scientific, 1998. 7922, 7941

Bijlsma, S.: On minimal-time ship routing, Ph.D. thesis, Delft University of Technology, Delft, 1975. 7914, 7917

Biran, A. and Pulido, R. L.: Ship Hydrostatics and Stability, Butterworth-Heinemann, 2013. 7931

Bowditch, C.: American Practical Navigator, Bicentennial Edition, 2002. 7929

Cessi, P., Pinardi, N., and Lyubartsev, V.: Energetics of semienclosed basins with two-layer flows at the strait, J. Phys. Oceanogr., 44, 967–979, 2014. 7959

Chen, H. H.: A dynamic program for minimum cost ship routing under uncertainty, Ph.D. thesis, Massachusetts Institute of Technology, 1978. 7916, 7917

Clementi, E., Oddo, P., Korres, G., Drudi, M., and Pinardi, N.: Coupled wave-ocean modelling system in the Mediterranean Sea, in: 13 International Workshop on Wave Hindcasting, Banff, Canada, 2013. 7939

De Dominicis, M., Pinardi, N., Zodiatis, G., and Lardner, R.: MEDSLIK-II, a Lagrangian marine surface oil spill model for short-term forecasting – Part 1: Theory, Geosci. Model Dev., 6, 1851–1869, doi:10.5194/gmd-6-1851-2013, 2013. 7937

Dijkstra, E. W.: A note on two problems in connexion with graphs, Numer. Math., 1.1, 269–271, 1959. 7923, 7941

Fenton, J. and McKee, W.: On calculating the lengths of water waves, Coast. Eng., 14, 499–513, 1990. 7936

Flannery, B. P., Press, W., Teukolsky, S., and Vetterling, W. T.: Numerical Recipes in FORTRAN 77: The Art of Scientific Computing, 1992. 7929

France, W. N., Levadou, M., Treakle, T. W., Paulling, J. R., Michel, R. K., and Moore, C.: An investigation of head-sea parametric rolling and its influence on container lashing systems, Mar. Technol., 40, 1–19, 2003. 7932

Francescutto, A. and Contento, G.: Bifurcations in ship rolling: experimental results and parameter identification technique, Ocean Eng., 26, 1095–1123, 1999. 7933

Gerritsma, J. and Beukelman, W.: Analysis of the resistance increase in waves of a fast cargo ship, Int. Shipbuild. Progr., 19, 285–293, 1972. 7927

Goldberg, A. V. and Harrelson, C.: Computing the shortest path: A search meets graph theory, in: Proceedings of the sixteenth annual ACM-SIAM symposium on Discrete algorithms, Society for Industrial and Applied Mathematics, 156–165, 2005. 7922

Gudmundsson, A.: Safety practices related to small fishing vessel stability, Tech. Rep., FAO, 2009. 7931

Hackett, B., Breivik, Ø., and Wettre, C.: Forecasting the drift of objects and substances in the ocean, in: Ocean Weather Forecasting, 507–523, Springer, 2006. 7938

Hagiwara, H.: Weather routing of(sail-assisted) motor vessels, Ph.D. Thesis, Technische Universiteit Delft, Delft, 1989. 7913, 7917

Hamilton, H. H.: Minimum-time ship routing by calculus of variations methods, M.S. Thesis, U.S. Naval Postgraduate School, Monterey, CA, 1962. 7914, 7917

IMO: Standards for ship manoeuvrability, 2002. 7931

IMO: Revised guidance to the master for avoiding dangerous situations in adverse weather and sea conditions, 2007. 7930, 7931, 7933, 7934, 7935

IMO: Adoption of the international code on intact stability, 2008. 7930

ITTC: Testing and Extrapolation Methods Propulsion, Performance Propulsion Test, Tech. Rep., International Towing Tank Conference, 2002. 7925

ITTC: 1978 ITTC Performance Prediction Method, Tech. Rep., International Towing Tank Conference, 2011a. 7927

ITTC: Prediction of Power Increase in Irregular Waves from Model Test, Tech. Rep., International Towing Tank Conference, 2011b. 7925

Journée, J.: Prediction of Speed and Behaviour of a Ship in a Sea-way, Tech. Rep., Delft University of Technology, Delft, 1976. 7925

Klompstra, M., Olsder, G., and Van Brunschot, P.: The isopone method in optimal control, Dynam. Control, 2, 281–301, 1992. 7914
Konak, A., Coit, D., and Smith, A.: Multi-objective optimization using genetic algorithms: a tutorial, Reliab. Eng. Syst. Safe., 91, 992–1007, 2006. 7916
Kosmas, O. T. and Vlachos, D. S.: Simulated annealing for optimal ship routing, Comput. Operations Res., 39, 576–581, 2012. 7916, 7917
Lawrence, J.: A Catalog of Special Plane Curves, Dover Books on Advanced Mathematics, Dover Publications, 1972. 7942
Levadou, M. and Gaillarde, G.: Proc. Int. Conf. on Design and Operation of Container Ships, 75–86, 2003. 7933
Lloyd, A.: Seakeeping – Ship Behaviour in Rough Seas, A. R. J. M. Lloyd, 1998. 7927, 7929, 7930
Lolla, T., Lermusiaux, P. F., Ueckermann, M. P., and Haley Jr, P. J.: Time-optimal path planning in dynamic flows using level set equations: theory and schemes, Ocean Dynam., 64, 1373–1397, 2014. 7915, 7917
Luenberger, D.: Introduction to Dynamic Systems: Theory, Models, and Applications, Wiley, 1979. 7914, 7916
MANDieselTurbo: Basic Principles of Ship Propulsion, Tech. Rep., MANDieselTurbo, 2011. 7925, 7926, 7929
Mannarini, G., Coppini, G., Oddo, P., and Pinardi, N.: A prototype of ship routing decision support system for an operational oceanographic service, TransNav, 7, 53–59, 2013. 7942
Mannarini, G., Lecci, R., and Coppini, G.: Introducing sailboats into ship routing system VISIR, in: 6th IEEE International Conference on Information, Intelligence, Systems and Applications, IEEE, accepted, 2015. 7947
Montes, A. A.: Network shortest path application for optimum track ship routing, Ph.D. thesis, Naval Postgraduate School, Monterey, CA, 2005. 7917
Nabergoj, R. and Prpić-Oršić, J.: A comparison of different methods for added Resistance Prediction, in: 22nd International Workshop on Water Waves and Floating Bodies, Plitvice/Croatia, vol. 18, 2007. 7930
Newman, J. N.: Marine Hydrodynamics, MIT Press, 1977. 7927, 7938
Oddo, P., Bonaduce, A., Pinardi, N., and Guarnieri, A.: Sensitivity of the Mediterranean sea level to atmospheric pressure and free surface elevation numerical formulation in NEMO, Geosci. Model Dev., 7, 3001–3015, doi:10.5194/gmd-7-3001-2014, 2014. 7939

Orda, A. and Rom, R.: Shortest-path and minimum-delay algorithms in networks with time-dependent edge-length, J. ACM, 37, 607–625, 1990. 7922, 7923
Perakis, A. and Papadakis, N.: Minimal time vessel routing in a time-dependent environment, Transport. Sci., 23, 266–276, 1989. 7914, 7915, 7917, 7929
Pinardi, N. and Coppini, G.: Preface "Operational oceanography in the Mediterranean Sea: the second stage of development", Ocean Sci., 6, 263–267, doi:10.5194/os-6-263-2010, 2010. 7939
Pontriagin, L., Boltyianskii, V., Gamkrelidze, R., and Mishchenko, E.: The Mathematical Theory of Control Processes, Interscience, 1962. 7914
Proctor, R. and Howarth, M.: Coastal Observatories and operational oceanography: a European perspective, Mar. Technol. Soc. J., 42, 10–13, 2008. 7912
Richardson, A., Bray, W., Sandström, R., Lokken, R., and Danaczko, M.: Advances in assessment of LNG sloshing for large membrane ships, in: Proceedings of the 21st International Conference and Exhibit, Gastech, 2005. 7931
Savitsky, D. and Brown, P. W.: Procedures for hydrodynamic evaluation of planing hulls in smooth and rough water, Mar. Technol., 13, 381–400, 1976. 7926, 7948
Shewchuk, J. R.: Delaunay refinement algorithms for triangular mesh generation, Comput. Geom., 22, 21–74, 2002. 7947
Spyrou, K.: Design criteria for parametric rolling, Ocean. Engin. Int., 9, 9, 11–27, 2005. 7932, 7933
Ström-Tejsen, J., Hugh, Y., and Moran, D.: Added resistance in waves, in: Society of Naval Architects and Marine Engineers, Transactions, 81, 109–143, 1973. 7927, 7928, 7932
Szlapczynska, J.: Multiobjective approach to weather routing, TransNav-Int. J. Mar. Nav. Safe. Sea Transport., 1, 273–278, 2007. 7916
Szlapczynska, J. and Smierzchalski, R.: Adopted isochrone method improving ship safety in weather routing with evolutionary approach, Int. J. Reliab., Qual. Safe. Engin., 14, 635–645, 2007. 7914, 7917
Takashima, K., Mezaoui, B., and Shoji, R.: On the fuel saving operation for coastal merchant ships using weather routing, Proc. Int. Symp. TransNav, 9, 431–436, 2009. 7916, 7917, 7938
Techy, L.: Optimal navigation in planar time-varying flow: Zermelo's problem revisited, Intell. Serv. Robot., 4, 271–283, 2011. 7914, 7915, 7917
Tolman, H. L.: User manual and system documentation of WAVEWATCH III TM version 3.14, Technical note, MMAB Contribution, 2009. 7938

Tonani, M., Oddo, P., Korres, G., Clementi, E., Dobricic, S., Drudi, M., Pistoia, J., Guarnieri, A., Romaniello, V., Girardi, G., Grandi, A., Bonaduce, A., and Pinardi, N.: The Mediterranean Forecasting System: recent developments, Geophys. Res. Abstr., EGU2014-16899-1, EGU General Assembly 2014, Vienna, Austria, 2014. 7939

Tonani, M., Balmaseda, M., Bertino, L., Blockley, E., Brassington, G., Davidson, F., Drillet, Y., Hogan, P., Kuragano, T., Lee, T., Mehra, A., Paranathara, F., Tanajurana, C. A. S., and Wang, H.: Status and future of global and regional ocean prediction systems, J. Oper. Ocean., doi:10.1080/1755876X.2015.1049892, in press, 2015. 7939

Triantafyllou, M. S. and Hover, F. S.: Maneuvering and Control of Marine Vehicles, Department of Ocean Eng., Massachussets Institute of Technology, Cambridge, USA, 2003. 7925

Umeda, N.: Nonlinear dynamics of ship capsizing due to broaching in following and quartering seas, J. Mar. Sci. Technol., 4, 16–26, 1999. 7930, 7935

Wei, S. and Zou, P.: Development of a 3D dynamic programming method for weather routing, Int. J. Mar. Navigat. Safe. Sea Transport., 6, 79–85, 2012. 7917

Yen, J. Y.: Finding the k shortest loopless paths in a network, Manage. Sci., 17, 712–716, 1971. 7922

Zeng, W. and Church, R.: Finding shortest paths on real road networks: the case for A*, Int. J. Geogr. Inf. Sci., 23, 531–543, 2009. 7922

Zhan, F. B. and Noon, C. E.: Shortest path algorithms: an evaluation using real road networks, Transport. Sci., 32, 65–73, 1998. 7922

Zoppoli, R.: Minimum-time routing as an N-stage decision process, J. Appl. Meteorol., 11, 429–435, 1972. 7916, 7917

Table 1. Graph notation and relevant graph quantities used in this paper. N_t is the number of time steps employed and is automatically adjusted by the model on the basis of the estimated voyage duration.

set name	$\mathcal{N}$	$\mathcal{E}$	$\mathcal{A}(t)$
set size	N	A	$A \times N_t$
element name	node	edge	edge weight
alias	gridpoint	link, arc, leg	edge delay
element symbol	j	(jk)	$a_{jk}(\ell)$
temporary node label	Y_j	-	-
permanent node label	X_j	-	-

Table 2. Parameters of the graph for the Mediterranean Sea after the removal of nodes and edges on the landmass (GSHHG coastline used). In the actual route computations, just a sub-domain of the whole basin is selected. Due to border effects, the connectivity ratio $A/N < 24$.

parameter	value	units
Top-left corner latitude	45.814	deg North
Top-left corner longitude	−6.000	deg East
Bottom-right corner latitude	30.234	deg North
Bottom-right corner latitude	36.240	deg East
Grid spacing	1/60	deg
Number of nodes, N	922 250	–
Number of edges, A	20 195 006	–
connectivity ratio, A/N	21.9	–

Table 3. Engine throttle levels employed in VISIR-I ($N_s = 7$).

s	1	2	3	4	5	6	7
$P^{(s)}/P_{\max}$ [%]	100	85	70	55	40	25	10

Table 4. Parameters of the ship model. The numerical factor in the formula for Fr value accounts for the conversion of speed v from kt to m s^{-1}; The values of η and φ_0 are just guesses. The value of ρ is taken from Cessi et al. (2014).

symbol	name	units	value
P	actually delivered engine power	hp	–
η	total propulsive efficiency	–	0.7
φ_0	φ spectral and directional average	–	0.5
ρ	sea surface water density	kg m^{-3}	1029
$\boldsymbol{R}_\mathrm{T}$	total resistance	kN	–
v	ship speed	kt	–
Fr	Froude Number		$\frac{0.52v}{\sqrt{g_0 L}}$
$\widetilde{Fr}$	reference Froude Number	–	–
$\boldsymbol{R}_\mathrm{c}$	calm water resistance	kN	–
$\boldsymbol{R}_\mathrm{aw}$	added wave resistance	kN	–
σ_aw	reduced added wave resistance	–	–

Table 5. Database of vessel propulsion parameters and principal particulars used in this work. See Fig. 3 for the meaning of the geometrical parameters. V1 is a ferryboat, while V2 is a fishing vessel. Most data stem from www.marinetraffic.com; T_R is estimated from the metacentric height GM using Weiss' method for small roll angles as reported in Benedict et al. (2004) and adding an extra 20 % to account for roll stabilization. Metacentric height is assumed to be GM = $2T/3$. Δ is not used by VISIR-I and is provided just for the sake of reference.

symbol	name	units	V1	V2
P_max	maximum engine brake power	hp	4000	650
c	ship top speed	kt	16.2	10.7
L	ship length at waterline	m	69	22
B	ship beam (width at waterline)	m	14	6
T	ship draught	m	3.4	2
T_R	ship natural roll period	s	9.8	5.4
GM	metacentric height	m	2.3	1.3
Δ	displacement	tons	550	90

Table 6. Ship and environmental parameters employed in the power balance equation Eq. (4) and in the inequalities for the safety constraints Eq. (5). Derived parameters such as T_E, $\widetilde{\sigma_{aw}}$ and $\widetilde{Fr}$ are omitted. For an explanation of symbols, see Table 8.

	Name of the condition		$\boldsymbol{p}_s$					$\boldsymbol{p}_e$			
$F_{eq}(\boldsymbol{v};\boldsymbol{p}_s,\boldsymbol{p}_e)=0$	Power balance equation		L	B	T	P_{max}	c		H_s		
$F_{ineq}(\boldsymbol{v};\boldsymbol{p}_s,\boldsymbol{p}_e)\le 0$	Safety constraints	Parametric roll	L		T_R			λ	H_s	T_w	
		Pure loss of stability	L					λ	H_s	T_w	θ_w
		Surfriding/Broaching-to	L					λ	H_s		θ_w

Table 7. List of main approximations done in VISIR-I.

Type	Title	Description/Comments	Paper section
Geometry	Linear discretization	grid step = 1 NM	2.2.1
Geometry	Angular discretization	resolution = 27°	2.2.1
Algorithm	1st shortest path only	alternative paths not computed	2.2.2
Algorithm	Forbidden waiting	sudden improvement in sea-state is ruled out	2.2.2
Algorithm	Throttle optimization	carried out prior to run of shortest path routine	2.2.3
Ship model	Power balance	no modelling of the propeller	2.3.1
Ship model	$\boldsymbol{R}_c$	residual resistance neglected	2.3.2
Ship model	$\boldsymbol{R}_{aw}$	not depending on wavelength	2.3.2
Ship model	$\boldsymbol{R}_{aw}$	not depending on angle between waves and ship course	2.3.2
Ship model	$\boldsymbol{\sigma}_{aw}$	linear dependence on Fr	2.3.2
Ship model	$\boldsymbol{R}_T$	displacement hull only	2.3.2
Ship model	Unlimited manoeuverability	turn radius not defined	2.3.2
Stability constraints	Simplified hull representation	parametrization coefficients not specialized on hull shape	2.3.3
Environmental Fields	Sea-over-land and downscaling	coastwise routes may be questionable	2.4.1

Table 8. Parameters of the environmental fields. $\theta_w = 0$ for northbound directions, increasing clockwise; $\alpha = 0$ for head seas, increasing clockwise, see Fig. 3.

symbol	name	units
H_s	significant wave height	m
$\zeta = H_s/2$	wave amplitude	m
λ	wavelength	m
H_s/λ	wave steepness	–
T_w	wave spectrum peak period	s
T_E	encounter wave period	s
θ_w	wave direction	radians
α	angle of wave encounter	radians
g_0	gravity acceleration	$m\,s^{-2}$
z	sea depth	m

Table 9. Coefficients of Eq. (50) for the computation of the geodetic and the optimal route. They are derived from least-square fits of VISIR-I performance on grids of size N in the range $[8 \times 10^1 - 8 \times 10^4]$. Used CPU type: Intel Xeon Processor 8Core E5-2670 2.6 GHz (running serially on a single core). Coefficient units are in s.

route type	c_0	c_1	c_2
geodetic	2.7×10^{-2}	2.2×10^{-4}	7.1×10^{-9}
optimal	4.3×10^{-2}	2.3×10^{-4}	7.3×10^{-9}

Table 10. Cycloidal benchmark: Length and duration of the three routes shown in Fig. 9. The free parameters in Eq. (51) are $\mathcal{R} = 14.6$ NM and $g = 10^{-3}\,\mathrm{m\,s^{-2}}$. Quantities in rows 2) and 5) refer to the numerical results using VISIR-I grid. Quantities in rows 3) and 6) are errors computed with respect to the values in the "Perfect cycloid" column of rows 2) and 5).

	Quantity	Route type	Units	Geodetic route	Optimal route	Perfect cycloid
1		analytic	–	$\mathcal{R}\sqrt{\pi^2+4}$	–	$4\mathcal{R}$
2	Length	VISIR-I	NM	54.6	59.5	58.4
3		error	%	−6.6	+1.9	0.0
4		analytic	–	$\sqrt{(\pi^2+4)\cdot\mathcal{R}/g}$	–	$\pi\sqrt{\mathcal{R}/g}$
5	J	VISIR-I	h	5 : 23	4 : 35	4 : 32
6		error	%	+18.7	+1.1	0.0

Table 11. Summary metrics for the case study routes displayed in Figs. 10–15. Values in bold between brackets for case study #3 refer to the optimal route without voluntary speed reduction (engine throttle forced to be always 100 %).

case #	Quantity	units	Geodetic route	Optimal route
1	Length	NM	127.5	131.6
	J	h	14 : 02	13 : 39
	Mean speed	kt	9.1	9.6
2	Length	NM	138.2	139.3
	J	h	14 : 56	14 : 53
	Mean speed	kt	9.3	9.4
3	Length	NM	270.4	277.4 (**285.1**)
	J	h	27 : 00	27 : 47 (**28:07**)
	Mean speed	kt	10.0	10.0 (**10.1**)

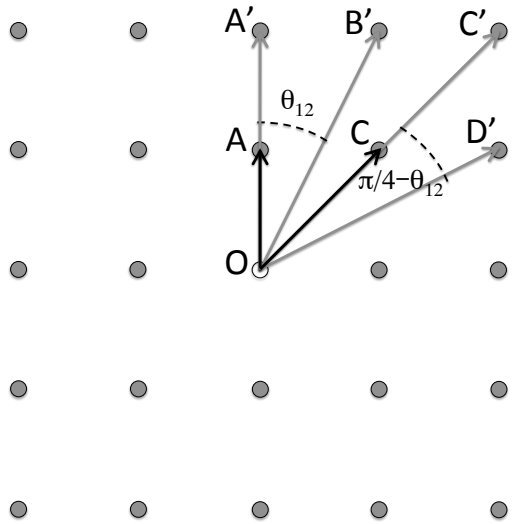

Figure 1. Graph spatial grid. Outgoing edges from the central node are displayed as arrows pointing to the respective tail node. Just the six edges relative to the first quadrant are shown (24-connectivity). The value of the angle θ_{12} is provided by Eq. (7).

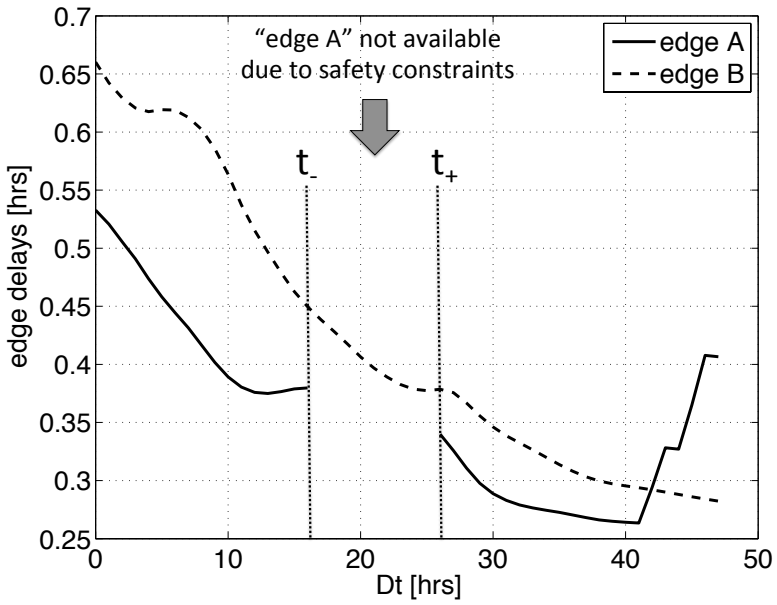

Figure 2. Examples of time dependent edge delays $a_{jk}(t)$. Here, FIFO condition Eq. (10) holds wherever $a_{jk}(t)$ is continuous (note that the y-range is about 1/100 of the x-range). The vertical dotted lines indicate the range $[t_-, t_+]$ of time Δt elapsed since departure, during which one of the edges is not available due to the navigational safety constraints.

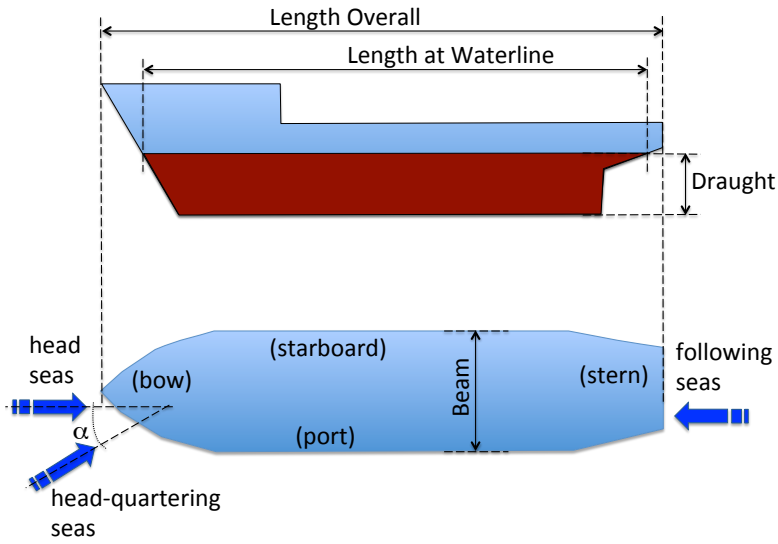

Figure 3. Main vessel dimensions and seaway nomenclature. The red part of the hull is normally underwater.

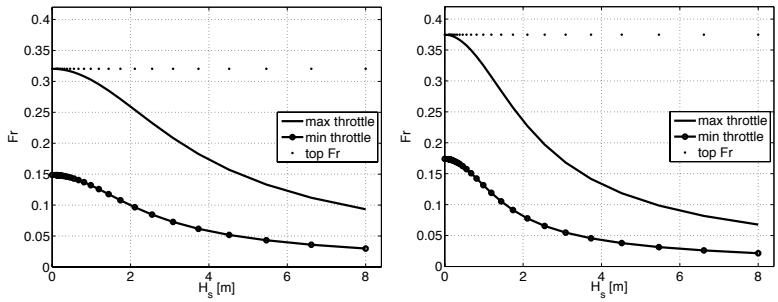

Figure 4. Sustained Froude number *Fr* at a constant engine throttle vs. significant wave height H_s. Both the cases of maximum (solid line) and minimum (line and dots) throttle of Table 3 are displayed. Left (right) panel refers to ship parameters for vessel V1(V2) in Table 5 respectively.

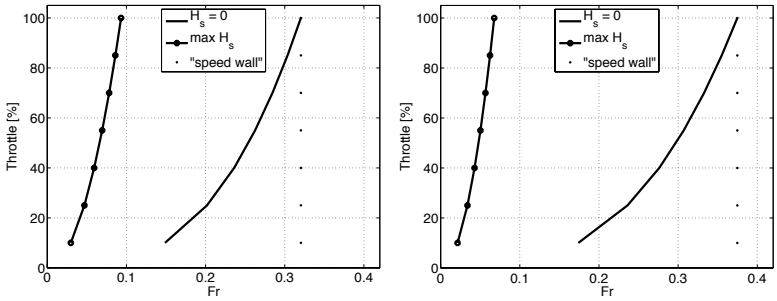

Figure 5. Engine throttle needed for sustaining a given *Fr*, in calm water resistance only ("H_s = 0") and both calm and wave added resistance ("max H_s", i.e., at maximum significant wave height seen in Fig. 4). Throttle values correspond to those of Table 3. Left (right) panel refers to ship parameters for vessel V1(V2) in Table 5 respectively.

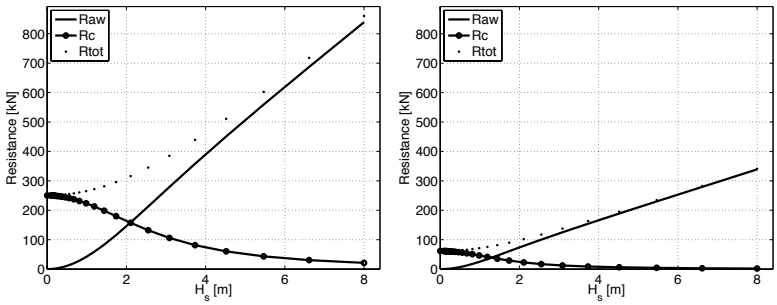

Figure 6. Resistance experienced by the vessel at constant power setting $P = P_{max}$ vs. significant wave height H_s. Calm water R_c, added wave resistance R_{aw} and their sum R_T are displayed. Left (right) panel refers to ship parameters for vessel V1(V2) in Table 5 respectively.

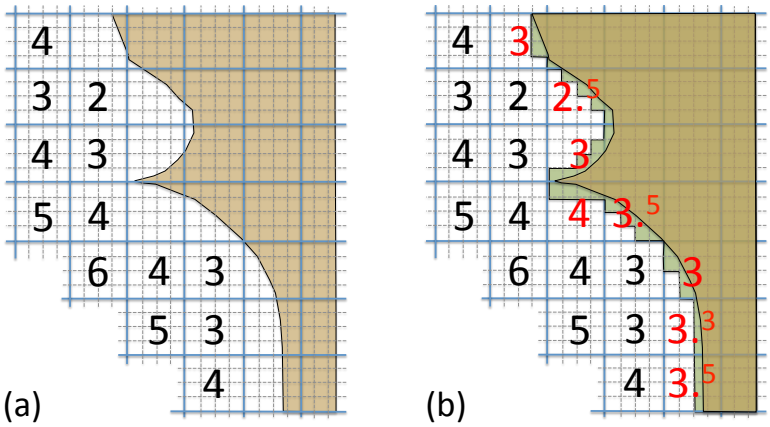

Figure 7. Sea-over-land extrapolation. **(a)** Numbers represent original field values, with coastline (black line) and landmass (brown area). **(b)** Field values after one sea-over-land iteration (replaced missing values are printed as red numbers). Target grid for the interpolation performed after application of sea-over-land is drawn as a dashed grid (for ease of presentation, it is drawn exactly four times finer than the original grid). Also shown in **(b)** is the land–sea mask of the target grid (green area).

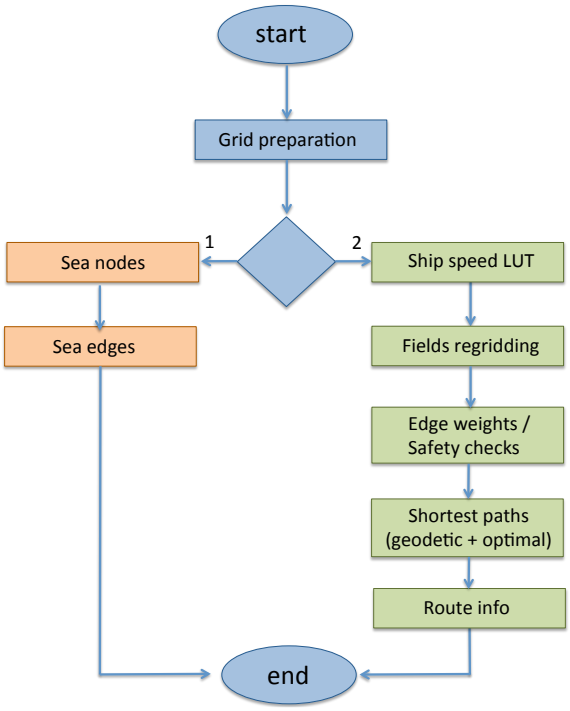

Figure 8. Flow chart of the computer code of VISIR-I model. Functioning mode (1) is run just once for preparing graph nodes and edges; mode (2) is the operational one, using sea nodes and edges computed from (1).

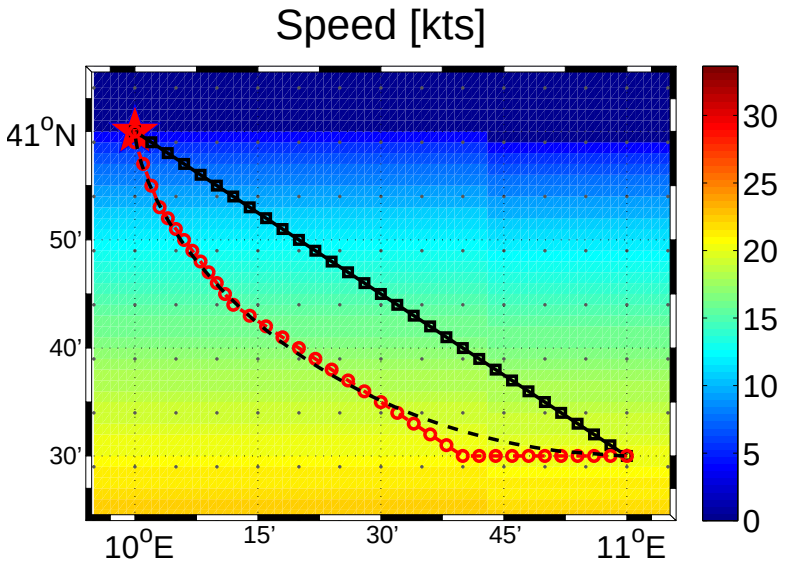

Figure 9. Cycloidal benchmark: Vessel speed $v(x,y) = \sqrt{2g(2\mathcal{R} - y)}$ is shown as a color background field (the feature at about 10°45′ E is due to the projection into spherical coordinates of a speed field constant along x). The geodetic and the optimal routes are displayed with squared black and circular red markers respectively. The analytical solution Eq. (51) (inverted cycloid) is plotted as a dashed black line. The length and duration of these three routes are compared in Table 10.

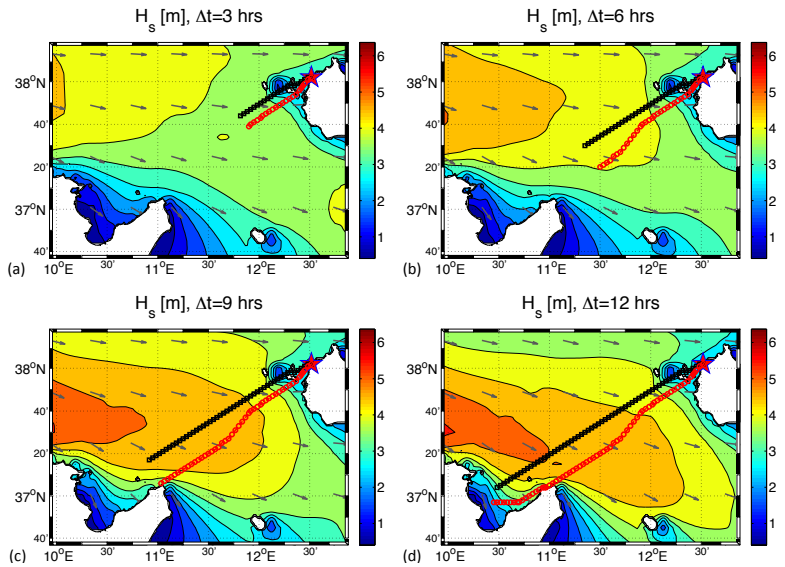

Figure 10. Case study #1. Geodetic (black markers) and optimal (red markers) route from Trapani (Italy) to Tunis (Tunisia) for vessel V1 of Table 5 and departure on 26 December 2013 at 21:00 UTC. **(a–d)** refer respectively to timesteps #4, 7, 10, 13 since departure. Significant wave height analysis fields H_s are displayed with coloured shadings and wave directions with arrows. As seen in Table 11, in this case, the geodetic route takes longer than the optimal route to reach the destination **(d)**.

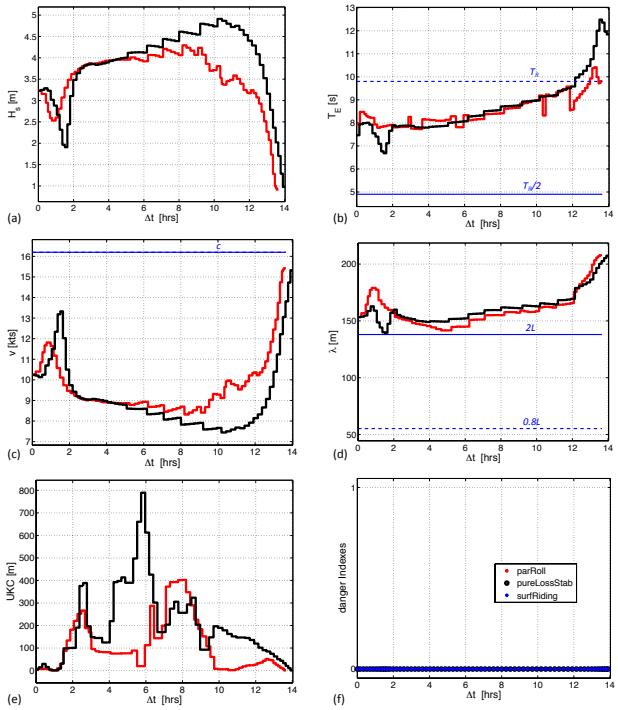

Figure 11. Case study #1. Information along geodetic (black) and optimal (red) route of Fig. 10: **(a)** significant wave height H_s; **(b)** encounter wave period T_E; **(c)** sustained speed v; **(d)** wavelength λ; **(e)** Under Keel Clearance UKC; **(f)** danger indexes along geodetic route, 0: safe; 1: dangerous. The quantities T_R, c, L refer to vessel V1 of Table 5.

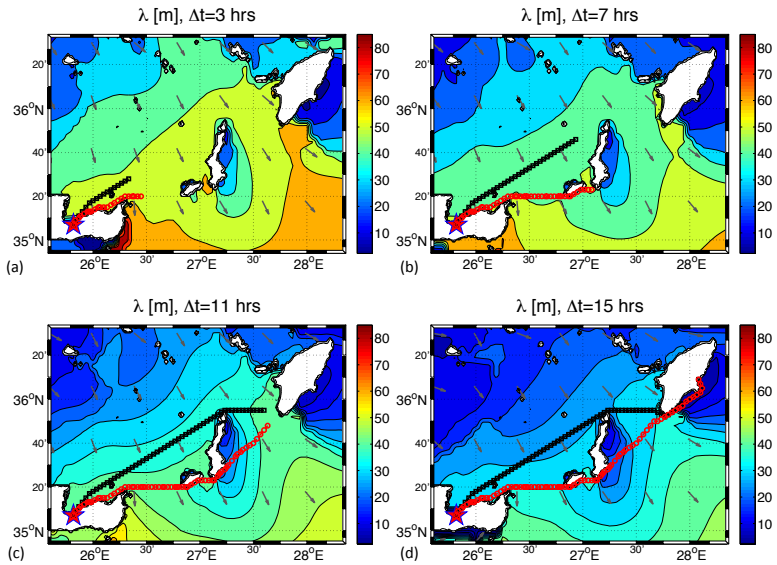

Figure 12. Case study #2. Geodetic (black markers) and optimal (red markers) route from Crete to Rhodes (Greece) for vessel V2 of Table 5 and departure on 20 September 2014 at 20:00 UTC. Panels **(a–d)** refer respectively to timesteps #4, 8, 12, 16 since departure. Wavelength analysis fields λ are displayed with coloured shadings and wave directions with arrows.

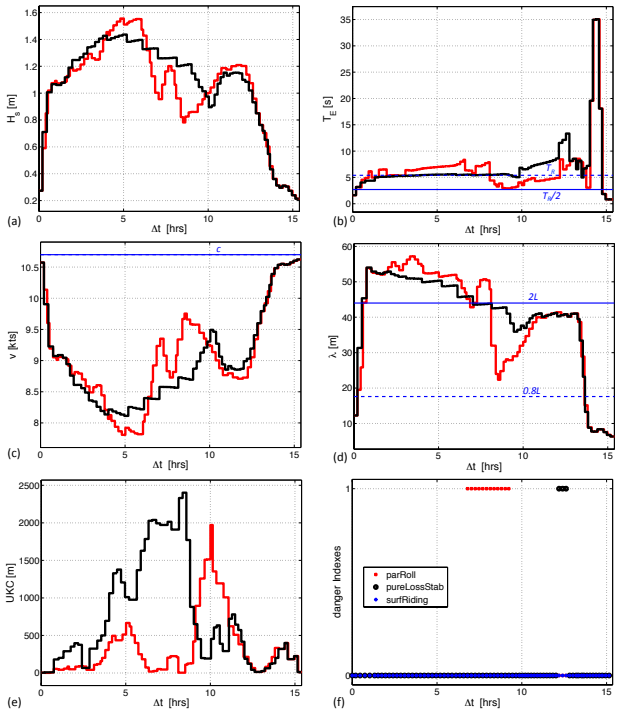

Figure 13. Case study #2. Information along geodetic (black) and optimal (red) route of Fig. 12: **(a)** significant wave height H_s; **(b)** encounter wave period T_E; **(c)** sustained speed v; **(d)** wavelength λ; **(e)** Under Keel Clearance UKC; **(f)** danger indexes along geodetic route, 0: safe; 1: dangerous. The quantities T_R, c, L refer to vessel V2 of Table 5.

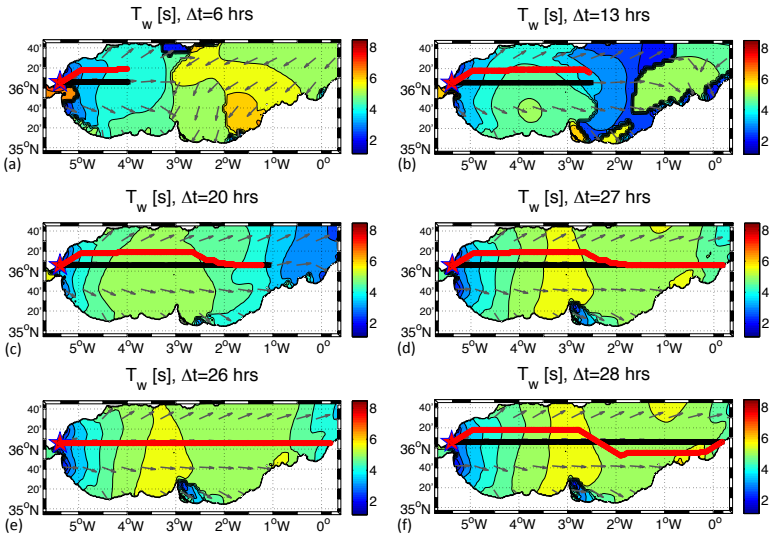

Figure 14. Case study #3. Geodetic (black markers) and optimal (red markers) route from Gibraltar (UK) to Ben Abdelmalek Ramdan (Algeria) for vessel V2 of Table 5 and departure on 5 October 2014 at 22:30 UTC. **(a–d)** refer respectively to timesteps #7, 14, 21, 28 since departure. **(e, f)** are respectively the last time step of a route with identical parameters but with the safety checks disabled **(e)** or voluntary throttle reduction disabled **(f)**. Wave period analysis fields T_w are displayed with colour shadings and wave directions with arrows.

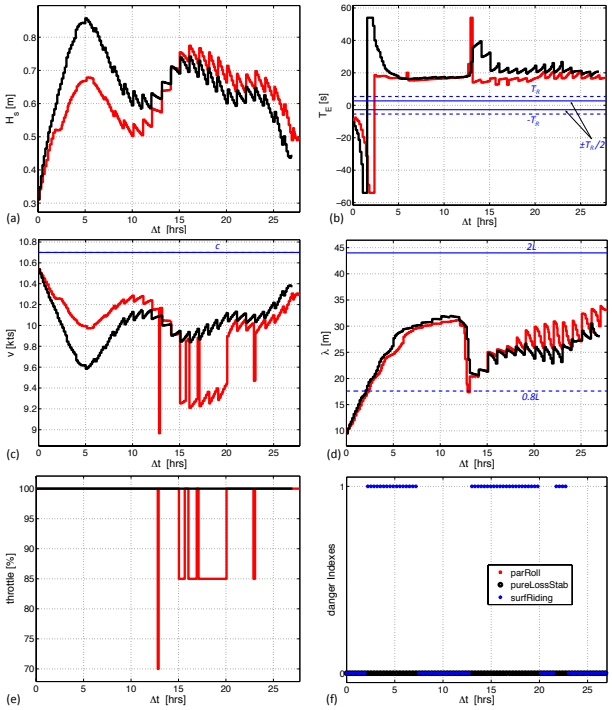

Figure 15. Case study #3. Information along geodetic (black) and optimal (red) route of Fig. 14: **(a)** significant wave height H_s; **(b)** encounter wave period T_E; **(c)** sustained speed v; **(d)** wavelength λ; **(e)** Engine throttle; **(f)** danger indexes along geodetic route, 0: safe; 1: dangerous. The quantities T_R, c, L refer to vessel V2 of Table 5.